

# Flat bands and compactons in mechanical lattices

Nathan Perchikov, O.V. Gendelman\*

*Faculty of Mechanical Engineering, Technion, Haifa 32000, Israel*

---

## Abstract

Local configurational symmetry in lattice structures may give rise to stationary, compact solutions, even in the absence of disorder and nonlinearity. These compact solutions are related to the existence of flat dispersion curves (bands). Nonlinearity can destabilize such compactons. One common flat-band-generating system is the 1D cross-stitch model, in which compactons were shown to exist for the photonic lattice case with Kerr nonlinearity. Smooth nonlinearity of this kind does not permit rigorous stability analysis for a chain. A mechanical system is suggested in which the nonlinearity is of the nonsmooth vibro-impact kind, for which the stability of the compacton solution can be addressed rigorously, using the notion of the saltation matrix for the analytic construction of the monodromy matrix, much as was recently done in the application of Floquet theory to discrete breathers. In addition, a smooth nonlinear lattice with linearly connected massless boxes containing two symmetric anharmonic oscillators each is proposed, where flat bands and compactons readily emerge. For this lattice, rigorous stability analysis is performed in the anti-continuum limit. In both systems, two nonlinear normal modes (NNMs) exist, one partially localized and one perfectly localized, namely the compacton and the discrete breather (DB) modes. Accordingly, two types of instability emerge. Local instability, related to internal resonance between the compacton and DB modes, and global instability, related to resonance of the stationary solution with the propagation frequencies. Consequently, two main types of bifurcations are observed. For the non-smooth system, global dynamics in the anti-continuum limit is examined and quasi-beating is observed.

*Keywords:* flat bands, compactons, vibro-impact potential, discrete breathers, Floquet theory

---

## 1. Introduction

The aim of the present research is to investigate the nonlinear dynamic phenomena related to presence of flat bands (FB) in the oscillatory spectra of mechanical and physical systems with special structural symmetry. Such structures are known to possess a number of unique and appealing physical and dynamical properties (intersecting oscillatory bands, perfectly localized discrete breathers, "hidden modes", which cannot be excited externally in a linear setting). Flat bands in physical systems have been observed and discussed in the recent literature to considerable extent. The effect of interactions and disorder on wave transport in periodic potentials, such as electrons in crystals, is

strongly amplified if the bandwidth (kinetic energy) is small. A particularly interesting situation arises when some of the dispersion bands become strictly flat with macroscopically degenerate eigenstates. In this limit, any relevant perturbation will lift the degeneracy and determine the emerging highly correlated and nontrivial eigenstates. In these systems it may be possible to control the interactions that successfully compete with kinetic energy and interesting wave transport phenomena may be produced. Engineering FB lattice models has been extended to three-dimensional (3D), two-dimensional (2D), and even one dimensional (1D) settings. A number of FB construction pathways using graph theory were suggested in the literature. An example is a case where compact states which are fully localized on several lattice sites are used. The origin of the compact flat band states (FBS) is the destructive interference effectively decoupling the FBS from the

---

\*Corresponding author

*Email address:* [ovgend@tx.technion.ac.il](mailto:ovgend@tx.technion.ac.il) (O.V. Gendelman)

rest of the lattice, similar to the known case where antisymmetric bound states embedded in and decoupled from the continuum are observed [1]. The context there is Fano lattices, the mechanism of resonance in which the notion of flat bands helps to explain. Fano lattices appear, for instance, in the context of plasmonics, which is relevant for laser technology, and also in the broader context of metamaterials [2]. An interesting feature of flat bands is that they are (still hypothetically) characterized by fractional power-law dependence between correlation length and level of disorder [3]. Flat bands have extremely singular densities of states, and therefore such systems are prone to form correlated states with broken symmetries [4]. One can also say that flat (dispersion) bands associated with propagation of waves in latticed materials occur when perfect destructive interference allows for compact localized eigenstates (CLS), or, modes with nonzero amplitude, only at a finite number of lattice sites [5]. This characterization of flat bands turns out to be closely related to the notion of discrete breathers. Discrete breathers (DBs) have long been a subject of both theoretical analysis and experimental studies [6, 7, 8]. Recently, it was demonstrated that one can derive exact solutions for DBs in vibro-impact chain models. Such lattices have been investigated analytically both for the Hamiltonian case [9] and for the forced-damped case [10]. Noteworthy in the perspective of the present research are the recent achievements in the analysis of FB structures, especially such as in [3] and [5], as well as the recent success in the analysis of the dynamics and stability of discrete breathers, in specific the analytic result presented in [10] and [11], mainly in what concerns the effects produced by nonlinearities.

In a spatially-extended system comprised of complex elements, the linear symmetry that produces flat dispersion bands implies that local dynamics can exist with no long-range interaction. This means that a single element can be excited locally.

Originally introduced for the spatially continuous case by Rosenau in [12] as nonlinear traveling waves of finite wavelength that preserve their shape after collisions with other compactons, emerging as solutions of a special class of nonlinear partial differential equations, due to an interplay between nonlinearity and dispersion, compactons have been since characterized also for discrete systems. In [13], a one-dimensional lattice of atoms with purely anharmonic interaction is considered, where a compacton solution is found analytically, characterized

by amplitude-independent width. Noteworthy is the establishment of a discrete compacton solution in the context of dynamic friction following the Frenkel-Kontorova model [14]. In [15] a strictly mechanical analog of the double-well nonlinear interaction potential that produces compacton-like solutions was constructed in the form of a lattice of pendula on an elastic foundation with strong coupling. It was found there that static compactons are stable whereas their mobile counterparts are unstable. In [16], exact results were obtained for linearly stable compactons on discrete 1D lattices with interaction of the Klein-Gordon type. In [17], a discrete chain with linear elastic interaction with the addition of non-smooth on-site potentials was examined in the context of emerging compactons.

In the recent work in [18] discrete systems were examined, both in one dimension (a chain) and in two dimensions (a rectangular array) using the Klein-Gordon model, with cubic nonlinearities both on-site and between sites. Exactly compact breather solutions were obtained, which are stable and non-traveling. In [19] discrete compact breathers were found in the context of Bose-Einstein condensates and nonlinear optics using various interaction models, such as the Discrete Non-Linear Schrödinger equation, as well as the Klein-Gordon and the Fermi-Pasta-Ulam models. The question of mobility of a discrete Soliton in the context of a practical application is addressed in [20] for a chain with a Peierls-Nabarro potential barrier typically used for dislocation movement in imperfect crystals. In [21] a discrete mechanical chain with Hertzian interaction is analyzed and traveling compactons with amplitude-independent wave-speed are established. In [22], DNA chains are studied using the Extended Discrete Nonlinear Schrödinger equation and solitary waves with compact support are obtained. Some of the obtained compactons are robust and some quickly decompose, depending on the DNA molecule model stacking parameters. A recent work, [23], deals with the problem of compactification by tuning parameters, such as the measure of interaction nonlinearity (the exponent in a power-law dependence), on-site energies and anisotropic coupling. Compact solitary waves are then obtained for three lattice-sites support, in the context of the Discrete Nonlinear Schrödinger equation.

In [24] flat bands and localized states were observed in 2D photonic Kagome lattices, with possible application to distortion-free image transmi-

tion. In [25] 1D and 2D diamond lattices were studied in the context of kinetic-energy-driven ferromagnetic transition in the Hubbard model using perturbation theory. The transition was found to be related to perturbed flat bands acquiring small dispersion allowing originally localized electrons to correlate. In [26], a photonic lattice is analyzed, where a flat band emerges due to PT (parity time) symmetry for specific gain and loss values which allows control over localization. In [27] a similar system is observed showing that both randomly positioned states and pinned states at the symmetry plane in the flat band can undergo thresholdless PT breaking. Furthermore the flat band is shown to be unaffected by weak disorder, unlike modes in the dispersive bands. In [28], a rhombic 1D optical waveguide lattice was analyzed with cubic nonlinearity and Flat band solutions were found to exist and become unstable due to mode coupling until a power threshold is reached. In [29], a dimerized Lieb lattice with next-nearest neighbor couplings was studied, a flat band was found, corresponding to a point-defect zero mode, spectrally isolated and spatially localized, producing a sublattice polarization, which provides a route to mode selection via loss imbalance. The revealed mechanism may be useful for photonic mode shaping and guiding, and possibly can be extended to laser settings. In artificial 2D materials the symmetry-breaking originating flat-band structure provides a mechanism to design robust defect states. In [30], scattering theory was applied to collisions in highly degenerate (flat) bands. It was shown how to construct localized states in flat bands that are scattering states of impurity potentials in 1D, particularized to a sawtooth lattice.

In [31] a planar composition of 2D square photonic lattices with Kerr nonlinearity (nonlinear dielectrics) constructing rotation corresponding to Pythagorean triples or co-rotated hexagonal lattices produces localization-delocalization-transition with stable thresholdless solitons. In [32] a stable flat band is observed in a rhombic quasi-1D lattice optical waveguide is observed in the presence of external driving. Robust localization is found to originate from destructive interference associated with the symmetry in the lattice geometry. Excitation of dispersive bands then leads to Bloch oscillations and coherent destruction of tunneling. In [33] a method is presented for the construction of different single and multiple flat bands using 1D optical lattices with configurational symmetry, such as

sawtooth and rhombic chains. Cubic Kerr-effect related nonlinearities and continuum-limit are also considered. Next-nearest neighbor and other extra interactions are used to create localization for specific power and coupling values. This is an example of existence of compactons in discrete nonlinear quantum lattices. A survey of different results related to local-support solutions in the aforementioned physical systems is given in [34].

It was recently shown in [35], that in a discrete mechanical system comprised of a massless box in harmonic on-site potential, with two identical oscillators inside, with cubic nonlinear interaction forces with the box, there exists a flat band corresponding to antisymmetric dynamics of the internal masses. The dynamics remains compact in a finite parameter range in the nonlinear regime. The present work shows, by numerical integration that the compacton solution remains stable also when for a chain of such elements. An additional noteworthy result is discussed in [36], where it is shown that there exist certain classes of lattices having configurational symmetry, a typical one being the so-called cross-stitch lattice, for which it is shown that Compact Localized States (of energy) exist corresponding to flat bands, where compact solution can be generated by accounting for permutations in the lattice-representing matrices.

The present work employs one such lattice, namely an augmented version of the 1D cross-stitch lattice. For this lattice it is rigorously shown that linearly stable immobile compacton solutions exist. The principal idea is to use the methodology of Floquet analysis employing analytically constructed saltation matrices, the way it was done for the case of discrete breathers, as in [11]. Both numerical and asymptotic analysis enabled by the vibro-impact potential model as checked for the DBs case is employed herein for compactons and the counterpart DB mode to examine stability.

The structure of the paper is as follows: Section 2 introduces and performs dispersion analysis of an augmented version of the cross-stitch model with non-smooth nonlinearity, Sections 3-4 perform rigorous stability analysis and numerical integration for the nonsmooth system, Section 5 performs linear analysis of a smooth chain of elements of the sort analyzed in [35] and briefly reviews the results therein regarding the nonlinear dynamics of a single element, Section 6 establishes the existence of stable compacton solutions for a chain by direct numerical integration, and Section 7 concludes.

## 2. Principal model system – (augmented) cross-stitch lattice with vibro-impact on-site potential

As a model system, we employ the the cross-stitch lattice discussed in [33] and [36], with the addition of identical shear springs of a generally different stiffness coefficient connecting the two chains site-to-site (rather than diagonally, as the cross-stitching). Furthermore, on-site vibro-impact potential with full restitution (elastic impacts) is added to each mass in the lattice, much like in [11]. The system is depicted in Fig. 1 below:

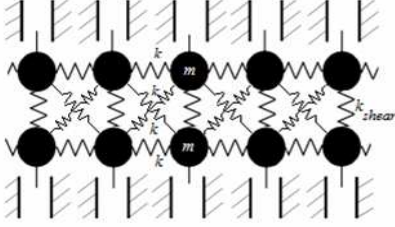


Fig. 1: Schematic picture of the basic setting

The equations of motion for the cross-stitch lattice given in Fig. 1 for the conservative case are as follows (where  $x_n(t), y_n(t)$  are horizontal displacements of the lower and upper chain elements, respectively):

$$\begin{aligned} \forall n \in \mathbb{N} \leq N_s : m\ddot{x}_n + k_{\text{shear}}(x_n - y_n) + k(4x_n - x_{n-1} - x_{n+1} - y_{n-1} - y_{n+1}) &= 0, \\ m\ddot{y}_n + k_{\text{shear}}(y_n - x_n) + k(4y_n - x_{n-1} - x_{n+1} - y_{n-1} - y_{n+1}) &= 0, \quad \forall |x_n|, |y_n| < \Delta; \\ \frac{\dot{y}_n|_{t|y_n| \rightarrow \Delta + \delta}}{\dot{y}_n|_{t|y_n| \rightarrow \Delta - \delta}} \xrightarrow{\delta \rightarrow 0} \frac{\dot{x}_n|_{t|x_n| \rightarrow \Delta + \delta}}{\dot{x}_n|_{t|x_n| \rightarrow \Delta - \delta}} \xrightarrow{\delta \rightarrow 0} -1 \end{aligned} \quad (1)$$

### 2.1. Linear dynamics

Taking a difference of the first two equations in Eq. (1), one obtains the equation of motion for the detached mode corresponding to the flat band:

$$m\ddot{v}_n + (4k + 2k_{\text{shear}})v_n = 0 \quad (2)$$

where

$$v_n \triangleq x_n - y_n, \quad \forall n \in \mathbb{N} \leq N_s \quad (3)$$

The flat band frequency is given by:

$$\omega_{FB} \triangleq \sqrt{\frac{4k + 2k_s}{m}} \quad (4)$$

Taking the sum of the two first equations in Eq. (1), one obtains the known equation of motion for a linear chain:

$$m\ddot{u}_n + k(4u_n - 2u_{n-1} - 2u_{n+1}) = 0 \quad (5)$$

where  $u_n \triangleq x_n + y_n, \quad \forall n \in \mathbb{N} \leq N_s$ . Dispersion analysis of Eq. (5), yields:

$$\omega_1(q) = 2\sqrt{\frac{k}{m}}(1 - \cos q)^{1/2} \quad (6)$$

Dispersion curves are given in Fig. 2, where one can observe intersection between the flat and the dispersive band (no self-avoidance as there is no linear coupling, unlike in [37]).

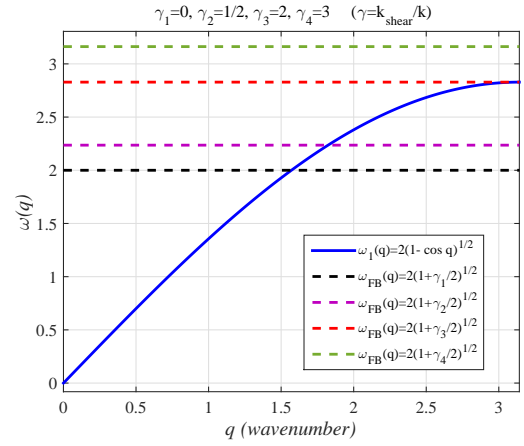


Fig. 2: Dispersion relations (frequencies given in units of  $\sqrt{k/m}$ )

For standard stability analysis of non-smooth systems [38], the system in the linear regime is best represented in the following vector form:

$$\mathbf{x}' = \mathbf{A}\mathbf{x} \quad (7)$$

where  $()'$  denotes differentiation with respect to time scaled by  $\sqrt{m/k}$  and:

$$\mathbf{A} \triangleq \begin{bmatrix} \mathbf{0} & \mathbf{I} \\ -\hat{\mathbf{A}} & \mathbf{0} \end{bmatrix} \quad (8)$$

in which  $\mathbf{0}$  is a matrix of zeros of size  $N \times N$ ,  $\mathbf{I}$  is the identity matrix of rank  $N$  and:

$$\begin{aligned} \hat{A}_{ij} &= (4 + \gamma)\delta_{ij} - \gamma\delta_{i,j+1}\langle N - 1 - j \rangle^0 \\ &- \gamma\delta_{i+1,j}\langle N - 1 - i \rangle^0 - \delta_{i,j+2}\langle N - 2 - j \rangle^0 \\ &- \delta_{i+2,j}\langle N - 2 - i \rangle^0 - \delta_{i,j+3}\langle N - 3 - j \rangle^0 \\ &- \delta_{i+3,j}\langle N - 3 - i \rangle^0 \end{aligned} \quad (9)$$

where  $\gamma \triangleq k_s/k$  (in which  $k_s \triangleq k_{\text{shear}}$ ), and:

$$\langle x \rangle^0 \triangleq \begin{cases} 1, & \forall x \geq 0 \\ 0, & \forall x < 0 \end{cases} \quad (10)$$

Also,  $N = 2N_s$ ,  $N_s$  being the number of sites.

### 2.2. Nonlinear regime

The nonlinear regime introduces conservative (perfect) impact, which can be represented by the following relation:

$$\mathbf{x}(t_i^+) = \mathbf{C}_j \mathbf{x}(t_i^-) \quad (11)$$

with  $t_i$  being the temporal series of impact instances (measured in units of  $\sqrt{m/k}$ ), and where:

$$\mathbf{C}_j \triangleq \begin{bmatrix} \mathbf{I} & \mathbf{0} \\ \mathbf{0} & \hat{\mathbf{C}}^{(j)} \end{bmatrix}, \quad \hat{\mathbf{C}}_{ik}^{(j)} \triangleq \delta_{ik} - 2\delta_{ik}\delta_{ij} \quad (12)$$

with  $j = 1, 2$  denoting the index of the particle at the localization cite.

## 3. Linear stability analysis

### 3.1. General framework

The monodromy matrix can be obtained as follows [38] (see Appendix A for details):

$$\mathbf{M} = (\mathbf{L}\mathbf{S}\mathbf{L})^2, \quad \mathbf{L} = \exp\left(\frac{\pi}{2\hat{\omega}}\mathbf{A}\right), \quad \mathbf{S} = \mathbf{S}_2\mathbf{S}_1 \quad (13)$$

where  $\hat{\omega} = \omega/\sqrt{k/m}$  is the normalized frequency of the periodic solution and:

$$\mathbf{S}_j = \mathbf{C}_j + (\mathbf{A}\mathbf{C}_j - \mathbf{C}_j\mathbf{A})\mathbf{D}_j, \quad j = 1, 2 \quad (14)$$

and

$$\mathbf{D}_1 \triangleq \frac{\mathbf{L}\mathbf{x}^0[\mathbf{n}^{(1)}]^\top}{[\mathbf{n}^{(1)}]^\top \mathbf{A}\mathbf{L}\mathbf{x}^0}, \quad \mathbf{D}_2 \triangleq \frac{\mathbf{C}_1\mathbf{L}\mathbf{x}^0[\mathbf{n}^{(2)}]^\top}{[\mathbf{n}^{(2)}]^\top \mathbf{A}\mathbf{C}_1\mathbf{L}\mathbf{x}^0} \quad (15)$$

where  $n_i^{(j)} = \delta_{ij}$  for  $j = 1, 2$ . Moreover, for compacton initial conditions:

$$x_i^0 = v_0(\delta_{N+1,i} - \delta_{N+2,i}) \quad (16)$$

where  $x_i^0$  is a generalized phase-space state vector, in which displacements are normalized by  $\Delta$  and velocities normalized by  $\Delta\sqrt{k/m}$ , and  $v_0$  represents the impact velocity normalized by  $\Delta\sqrt{k/m}$ .

### 3.2. Analytical integration of the compacton solution

For the compacton solution one has:

$$v_i(t) = \frac{1}{2}v_1(t)\delta_{1i} \quad (17)$$

where  $v_i(t)$  is as defined in Eq. (3), only normalized by  $\Delta$ , and where:

$$v_1(t) = \pi S_0^{-1} \left| \pi - 2\pi \left\{ \frac{\omega t}{2\pi} \right\}_{\text{frac}} \right| \quad (18)$$

$$S_0 \triangleq \sum_{n=1,3,5}^{\infty} [(\hat{\omega}^2 n^2 - 4)^2 - 16]^{-1/2} \quad (19)$$

and  $\{z\}_{\text{frac}} = z - [z]$ .

### 3.3. Compacton mode stability bounds – asymptotic results

*The  $\gamma \ll 1$  case.* It is possible to obtain analytic estimates of the stability bounds for the stable existence of the compact solution, borrowing from the compactness of the solution. A chain of three two-mass elements is considered. The central element corresponds to the energy-containing part. The two neighbors are necessary in order to account for the simplest perturbation to the compact solution. The monodromy matrix for this three-element system, containing six masses and having the dimension of  $12 \times 12$ , can be constructed analytically. Furthermore, the matrix can be expanded for small values of  $\gamma$ . Order balancing then requires that the period  $\hat{\omega}$  be expanded in powers of the stiffness ratio as well. Next, analytical calculation of the spectral norm of the monodromy matrix in leading-orders asymptotics produces the following expression:

$$|\lambda|_{\max} \xrightarrow{\gamma \rightarrow 0} 1 + 4\sqrt{\frac{2}{3}}q_0\sqrt{3 - 4q_0^2\gamma} + \mathcal{O}(\gamma^2) \quad (20)$$

where  $q_0$  emerges from orders-balancing as:

$$q_0 \triangleq \frac{\pi}{4} \left( \frac{\omega}{\omega_{FB}} \right)^{-1} \gamma^{-1/2} \quad (21)$$

The critical value rendering the spectral norm of the monodromy bounded by unity is thus:

$$q_0^{\text{cr}} = \frac{\sqrt{3}}{2} \quad (22)$$

which corresponds to the following stability-bounding asymptotic relation in the frequency–stiffness-ratio plane:

$$\frac{\omega_{cr}}{\omega_{FB}} \xrightarrow{\gamma \rightarrow 0} \frac{\pi}{2\sqrt{3}} \gamma^{-1/2} \quad (23)$$

Since this critical value corresponds to transition from a pair of complex conjugate eigenvalues on the unit circle to a pair of real reciprocal eigenvalues, one would expect a pitchfork bifurcation in the underlying chain at this stability bound. Fig. 3 shows the agreement between numerical calculation of the stability map for the compacton solution and the asymptotic estimate.

*The  $\gamma \gg 1$  case.* The  $\gamma \gg 1$  case is the anti-continuum limit in which the chain decouples and one effectively has a single ‘molecule’ comprised of two masses in vibro-impact potential connected by a linear spring. The stability of the antisymmetric mode of vibration can be investigated analytically. It turns out that two eigenvalues of the corresponding monodromy matrix are equal to unity and two additional eigenvalues, with a product of unity exist. The smallest of these two is treated here for presentational reasons. It appears that this eigenvalue depends only on a certain combination of the two parameters of the problem, namely  $\gamma$  and  $\hat{\omega}$ , and not on both of them independently. A plot of the dependence of the critical eigenvalue on that combination reveals that the system is always unstable in this limit, as can be learned from Fig. 4. Moreover, calculation of the eigenvector of the monodromy matrix of the full chain (in the middle of the feasible range-of-change of the aforementioned combination of parameters) reveals strict localization (as one might expect by naïve understanding of the considered limit). This is shown in Fig. 5 .

### 3.4. Compacton mode stability bounds – numeric results

Numerical spectral analysis of analytically constructed monodromy matrices for different stiffness-ratio/frequency pairs, reveals the existence of a growing stable stripe, with upper and lower bounds, for decreasing shear-spring stiffness. The upper (frequency) stability limit corresponds to pitchfork bifurcation. The lower stability limit corresponds to the Neimark-Sacker bifurcation. The bounds, along with corresponding asymptotic estimates and the flat band as a reference, are shown in Fig. 3.

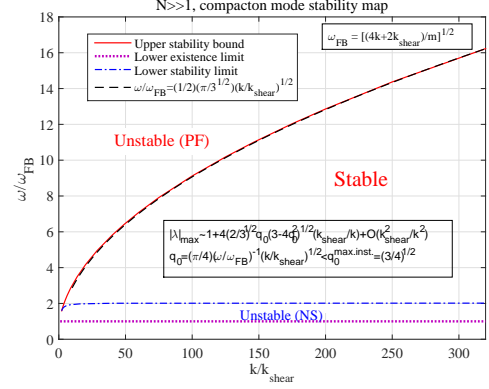


Fig. 3: Compacton mode stability bounds – numeric results in solid (red online) and dash-dot (blue online) and analytic results in dash black

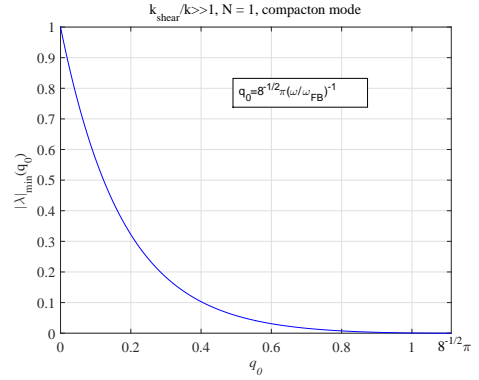


Fig. 4: Critical Floquet multiplier variation ( $\gamma \gg 1$ )

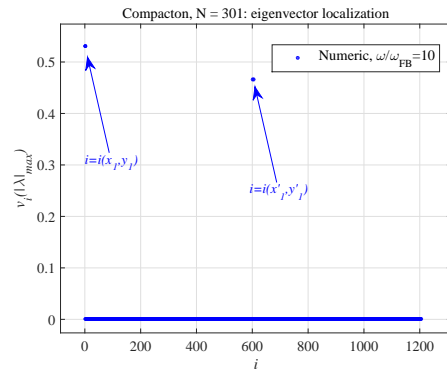


Fig. 5: Typical  $\gamma \gg 1$  limit full chain monodromy eigenvector showing localization

### 3.5. Analytical integration of the breather solution

In the symmetric mode the two chains move simultaneously. Therefore, essentially, the periodic solution is a breather in a conservative linearly-linked on-site vibro-impact chain. It is treated in [39], but is analyzed here in a more compact form. The effective breather displacement, namely,  $u_n(t) \triangleq x_n(t) + y_n(t)$  is given by:

$$u_n(t) = \sum_{l=1}^{\infty} \hat{V}_{nl} \cos[(2l+1)\omega t] \quad (24)$$

where

$$\hat{V}_{1,l} \triangleq \left( \bar{\alpha}_l \hat{\alpha}_l^2 \hat{W}_{1l} + \hat{\alpha}_l \bar{\alpha}_l^2 \hat{W}_{2l} \right) p \quad (25)$$

$$\hat{V}_{n \neq 1,l} \triangleq \left( \hat{\alpha}_l^n \hat{W}_{1l} + \bar{\alpha}_l^n \hat{W}_{2l} \right) p \quad (26)$$

$$p \triangleq \Delta \left[ \sum_{l=1}^{\infty} \left( \bar{\alpha}_l \hat{\alpha}_l^2 \hat{W}_{1l} + \hat{\alpha}_l \bar{\alpha}_l^2 \hat{W}_{2l} \right) \right]^{-1} \quad (27)$$

where  $\Delta$  is the amplitude of the breather, or half the distance between the limiters.

$$A_l \triangleq \frac{\hat{\alpha}_l^3 2\alpha_l \hat{\alpha}_l^{N_s-3} - \hat{\alpha}_l^{N_s-4} - \bar{\alpha}_l / \hat{\alpha}_l}{\bar{\alpha}_l^3 2\alpha_l \bar{\alpha}_l^{N_s-3} - \bar{\alpha}_l^{N_s-4} - \hat{\alpha}_l / \bar{\alpha}_l} \quad (28)$$

$$B_l \triangleq A_l \left[ \left( 4\alpha_l^2 - 2\frac{\alpha_l}{\bar{\alpha}_l} - 1 \right) \bar{\alpha}_l^{N_s} - \bar{\alpha}_l^2 \right] - \left[ \left( 4\alpha_l^2 - 2\frac{\alpha_l}{\hat{\alpha}_l} - 1 \right) \hat{\alpha}_l^{N_s} - \hat{\alpha}_l^2 \right] \quad (29)$$

$$\hat{W}_{1l} \triangleq \frac{2}{\pi} B_l^{-1}, \quad \hat{W}_{2l} \triangleq -A_l \hat{W}_{1l} \quad (30)$$

$$\hat{\alpha}_l \triangleq \alpha_l + \sqrt{\alpha_l^2 - 1}, \quad \bar{\alpha}_l \triangleq \alpha_l - \sqrt{\alpha_l^2 - 1} \quad (31)$$

$$\alpha_l \triangleq 1 - \hat{\omega}^2(l+1/2)^2 \quad (32)$$

The initial conditions for stability analysis of the breather mode are zero displacements with consistent initial velocities, namely:

$$u_n(t=t_0) = 0, v_n(t=t_0) = 0, \dot{v}_n(t=t_0) = 0 \quad (33)$$

and the following consistent (inhomogeneous) initial condition, with  $t_0 = \pi/(2\omega)$ :

$$\dot{u}_n(t=t_0) = -\omega \sum_{l=1}^{\infty} (-1)^l (2l+1) \hat{V}_{nl} \quad (34)$$

### 3.6. Breather mode stability bounds – asymptotic results

*The  $\gamma \ll 1$  case.* Analytic estimation of the stability bounds of the breather mode in the  $\omega$ - $\gamma$  plane can be obtained asymptotically for  $\gamma \ll 1$ . To this end, once again a triple of two-mass molecules is considered. This is the smallest chain needed to represent a symmetric system with periodic boundary conditions. As in the case of the compacton mode, the stability criterion here prescribes an order of unity critical value on a combination of the parameters. One of these parameters is assumed asymptotically small, hence it is expected that the other parameter (here the frequency) would be of order different than unity in the critical case. Clearly, the frequency cannot be much smaller than the linear-regime limit, and thus a large critical value is expected. Unlike in the case of the compacton mode stability analysis, where there is only one velocity value in the analysis, which thus cancels-out, in the case of the breather the exact initial velocity profile is required. For the asymptotic analysis considered here the high-frequency limit of Eq. (34) for  $N_s = 3$ , as obtained by rigorous asymptotic treatment, is sufficient and reads:

$$\hat{q} \triangleq \frac{\pi}{2\hat{\omega}}, \quad \dot{u}_1|_{t_0} = -\hat{q}^{-1}, \quad \dot{u}_{2,3}|_{t_0} = \hat{q} \quad (35)$$

Having all the quantities required for the construction of the monodromy matrix (as functions of  $\gamma$  and  $\omega$ ), one can obtain it analytically. Assuming  $N_s = 3$  and performing second order asymptotic expansion with respect to the small parameters  $\gamma$  and  $q$ , the critical eigenvalue can be presented as follows:

$$|\lambda|_{\max} \xrightarrow{\gamma \rightarrow 0} 1 + 4\sqrt{\frac{2}{3}} q_1 \sqrt{4q_1^2 - 3\gamma - 16q_1^2 \gamma^2} \quad (36)$$

where  $q_1$  is:

$$q_1 \triangleq \frac{\pi}{\sqrt{32}} \left( \frac{\omega}{\omega_{\text{prop}}} \right)^{-1} \gamma^{-1/2} \quad (37)$$

and

$$\omega_{\text{prop}} \triangleq \max_q [\omega_1(q)] = \sqrt{8k/m} \quad (38)$$

The critical value rendering the spectral norm of the monodromy matrix bounded by unity is the same as for the compacton:

$$q_1^{\text{cr}} = \frac{\sqrt{3}}{2} \quad (39)$$

This corresponds to the following stability-bounding asymptotic relation in the frequency–stiffness-ratio plane:

$$\frac{\omega_{\text{cr}}}{\omega_{\text{prop}}} \xrightarrow{\gamma \rightarrow 0} \frac{\pi}{2\sqrt{6}} \gamma^{-1/2} \quad (40)$$

One notes that in the  $\gamma \rightarrow 0$  limit, the same curve in the  $\omega$ – $\gamma$  plane is obtained as the stability limit for either the compacton or the breather, with the compacton mode being stable below that line and the breather mode being stable above it, as arises from Eqs. (4,6,20,23,36,40).

*The  $\gamma \gg 1$  case.* In the limit of large  $\gamma$ , the cross-stitch chain degenerates to a single two-mass molecule. The stability of the symmetric mode of vibration of such a molecule can be examined analytically. It appears that once the assumption of large  $\gamma$  allows to consider a single two-mass element, no further asymptotic is required, and the eigenvalues of the monodromy matrix can be obtained in closed-form. Two eigenvalues are identically unity, which represents the degeneracy in position and velocity arising from the symmetry. Two additional eigenvalues are generally complex conjugates with absolute values of unity. Those eigenvalues are the critical ones:

$$\lambda_{\text{cr}} = e^{\pm i\pi\sqrt{\gamma}\left(\frac{\omega}{\omega_{\text{prop}}}\right)^{-1}} \quad (41)$$

This result is a first-order approximation in  $\gamma^{-1}$ . Clearly higher terms would perturb those eigenvalues. For eigenvalues with nonzero imaginary parts, the perturbation could only change the angles of the eigenvalues in the complex plane, since symmetry would keep them complex conjugate (with the same radii) and energy conservation would keep the product of their radii at the value of unity. Hence, they would both remain on the unit circle, and no instability would occur. However, for the special case where all four eigenvalues are equal to unity, a small perturbation can drive two of them apart on the real axis, keeping their product unitary. In this case one eigenvalue would be real and greater than unity, corresponding to instability. Therefore, an infinite (countable) set of narrow instability tongues (turning to lines for  $\gamma \rightarrow \infty$ ) would emerge on the  $\omega$ – $\gamma$  plane in the perturbed (chain) case, obeying the following asymptotic behavior:

$$\frac{\omega_{\text{cr}}}{\omega_{\text{prop}}} \xrightarrow{\gamma \rightarrow \infty} \frac{\sqrt{\gamma}}{2\mathcal{N}}, \quad \forall \mathcal{N} \in \mathbb{N} \quad (42)$$

The quality of the asymptotic estimates for the stability bounds is shown in Figs. 6 and 7. Fig. 7

also features a lower stability bound, corresponding to double pitchfork bifurcation. In that case, both chains experience the pitchfork-type loss of stability simultaneously, which implies the destruction of periodicity for the breather. This differs from the regular pitchfork bifurcation emerging for the upper bounds, where stability is lost due to internal resonance, as part of the energy is transmitted from the symmetric to the antisymmetric mode.

### 3.7. Breather mode stability bounds – numeric results

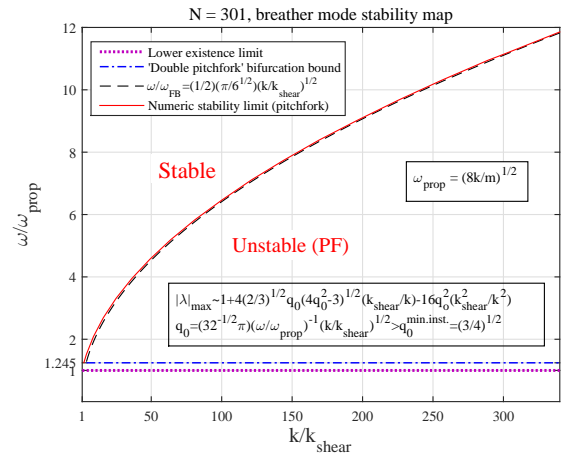


Fig. 6: Breather mode stability bounds for  $\gamma \ll 1$  (asymptotic estimate shown in dash)

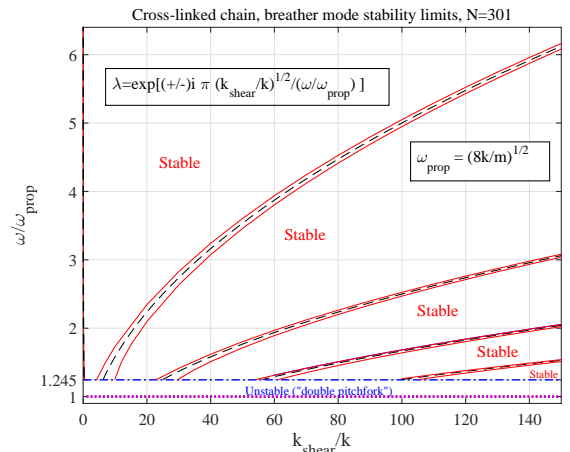


Fig. 7: Breather mode stability bounds for  $\gamma \gg 1$  (asymptotic estimate shown in dash)

## 4. Numerical integration

Although the most powerful result obtained by choosing a non-smooth model system is the rigorous linear stability analysis, clearly validation by direct numerical integration is called for. To this end, an algorithmically stable integration scheme is employed, in conjunction with a smooth model representing the vibro-impact potential, which is required for the algorithmic stability. The widely-known high-odd-power force term is used for impact modeling. The solver employed here is a one-step method based on the trapezoidal rule and a backward differentiation formula of order 2 with a free interpolant [40].

### 4.1. Compacton IC in and below the stable region

Integration with a stable energy-conserving scheme, modeling the elastic impacts by high odd-power force terms in the form:

$$\ddot{\mathbf{w}} = -\hat{\mathbf{A}}\mathbf{w} - \tilde{\mathbf{f}} \quad (43)$$

where  $\hat{\mathbf{A}}$  is defined in Eq. (9), the displacements vector is:  $\mathbf{w} = (x_1, y_1, x_2, y_2, \dots, x_{N_s}, y_{N_s})^\top$ , and the nonlinear impact-representing forcing vector is:

$$\tilde{f}_i \triangleq (2\xi + 1)w_i^{4\xi+1} \quad (44)$$

where  $\xi$  is potential-sharpness, reproducing impact when  $\xi \rightarrow \infty$ . As in [11],  $\xi = 300$  was chosen here.

Fig. 8, along with Fig. 3, comprises, perhaps, the most important result in the present paper. It confirms the existence of a stable compacton in a nonlinear 1D lattice, by showing the dynamic boundedness of a perturbation to a perfectly compact solution. This is illustrated both by the histories of the principal-site displacements and by the chain mode-amplitude profiles.

Fig. 9 shows that when the frequency is smaller than the critical (lower) bound, delocalization occurs, through a Neimark-Sacker bifurcation, leading to (arguably) chaotic trajectories. The starting state there is the same slightly perturbed compact initial condition as in the case exhibited in Fig. 8. In both cases, the shear spring is taken to be an order of magnitude less rigid than the other springs. This is (obviously) required for a stable solution to be feasible according to linear stability analysis.

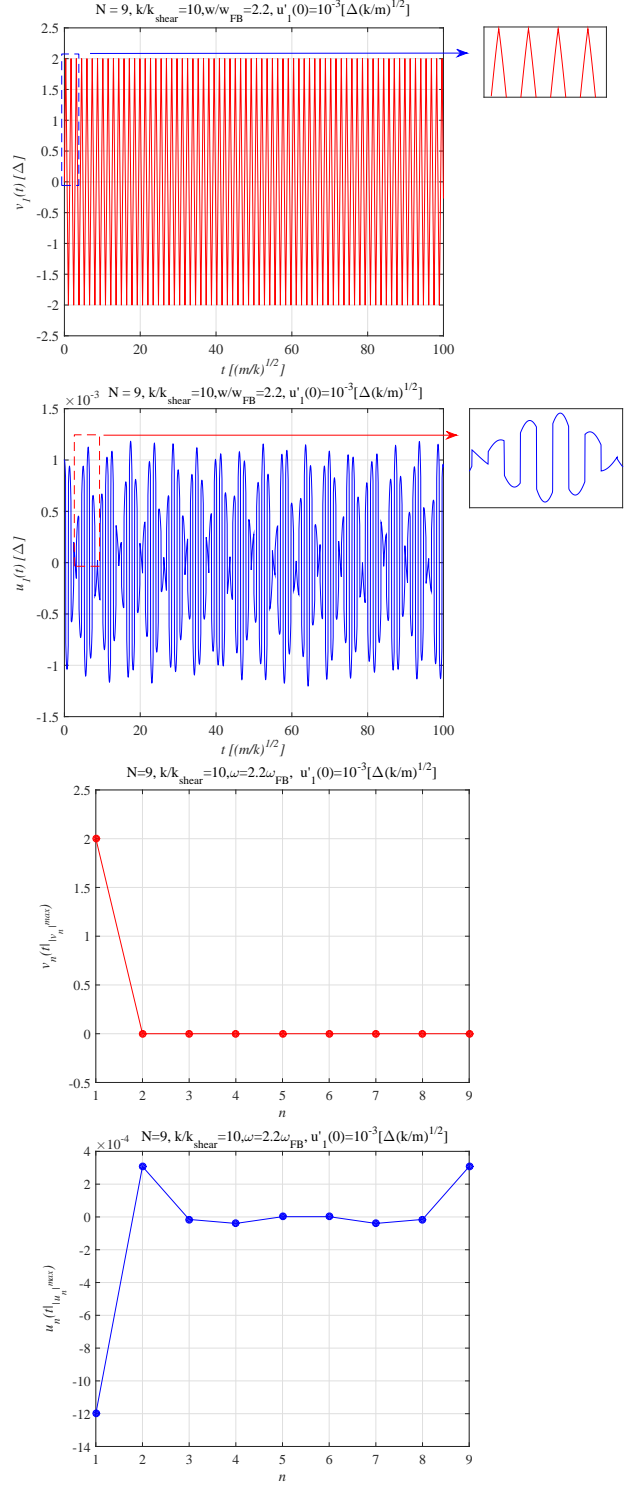


Fig. 8: Compacton integration results – stable case

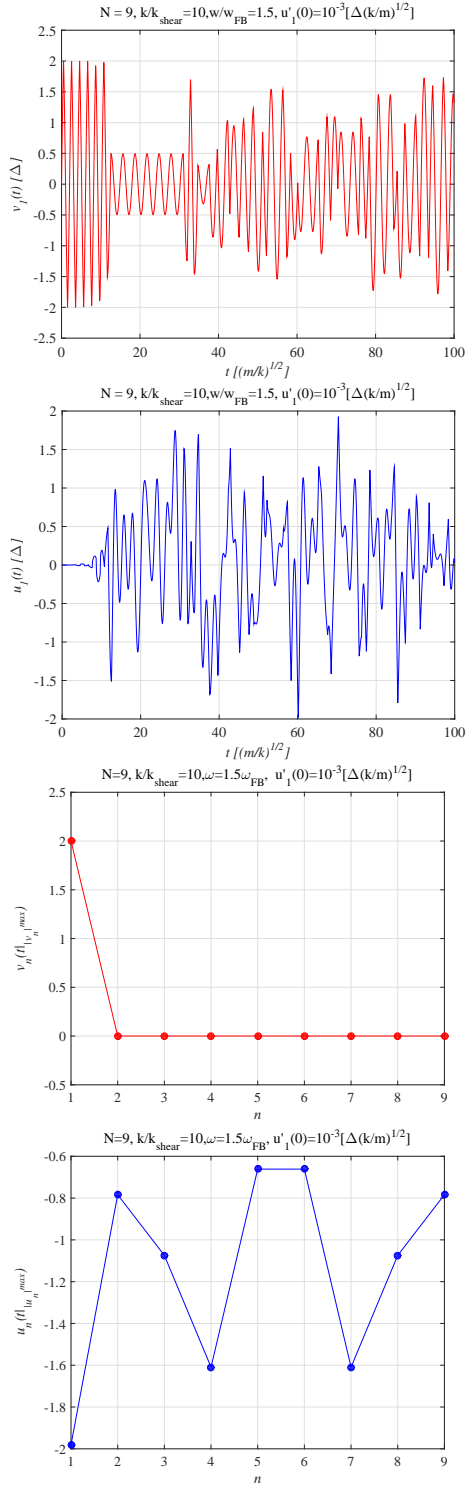


Fig. 9: Compacton integration results – 'NS' unstable case

#### 4.2. Breather IC in and below the stable region

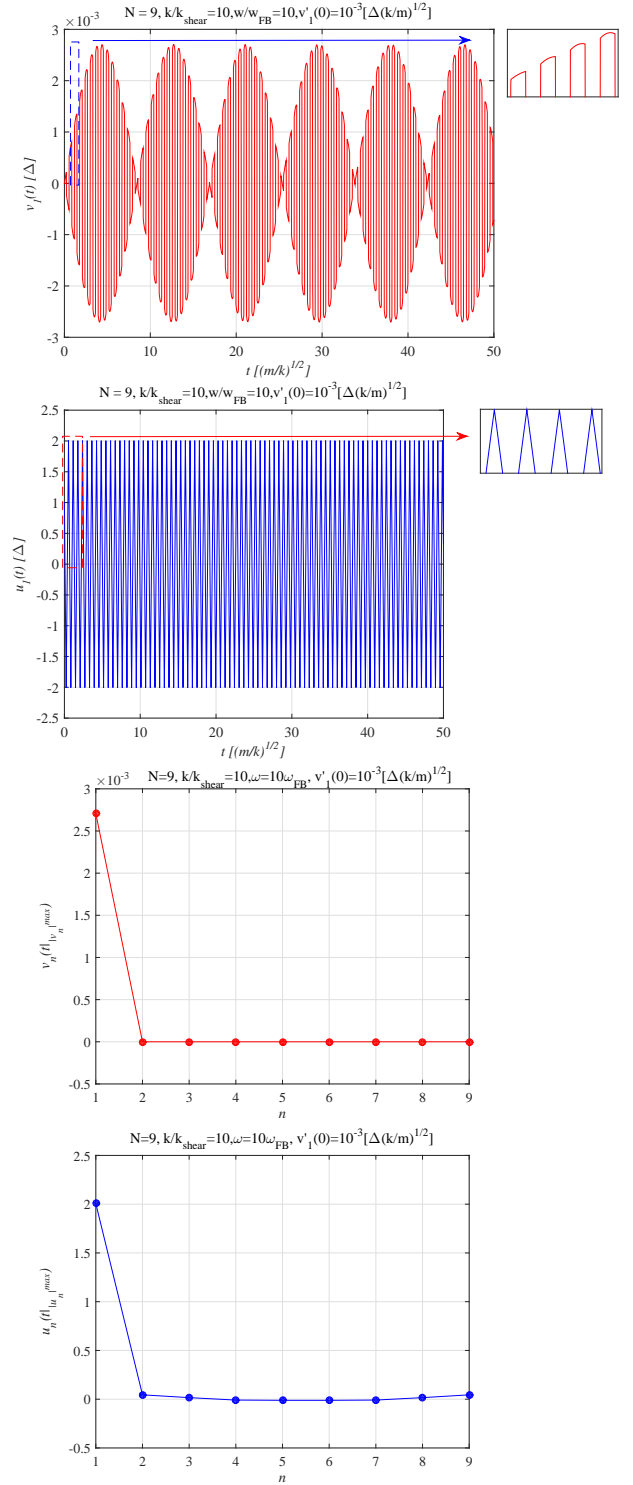


Fig. 10: Breather integration results – stable case

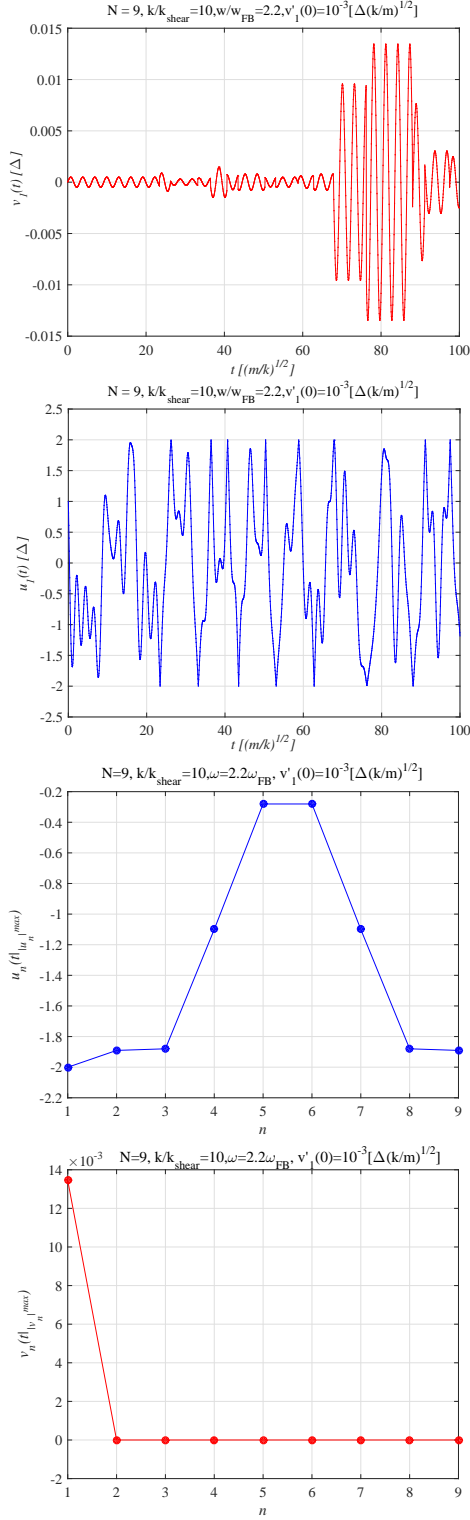


Fig. 11: Breather integration results – 'PF' unstable case

Fig. 10 confirms the stability of the breather for a frequency value above the linear stability (lower) bound (and stiffness ratio the taken same as before). Noteworthy is the absence of an upper energy (frequency) stability bound. As may be expected, small perturbation of the zero solution for the antisymmetric mode stays small in amplitude, spatially localized and temporally periodic. Fig. 11 illustrates the loss of stability of the breather mode for a frequency lower than the critical value. This confirms the linear stability analysis, which predicts loss of stability here, through pitchfork bifurcation. The long-time dynamics of the perturbed modes seems chaotic and not un-resembling the one emerging from the 'NS' bifurcation shown in Fig. 9.

#### 4.3. Compacton IC above the stable region – global dynamics

Asymptotic analysis reveals that for the breather mode:

$$|\dot{u}_n(t)| \underset{q \rightarrow 0}{\leq} \hat{q}^2 |\dot{u}_1(t)| \quad (45)$$

(where  $\hat{q}$  is as defined in Eq. (35)), which implies asymptotic compactness of the breather mode.

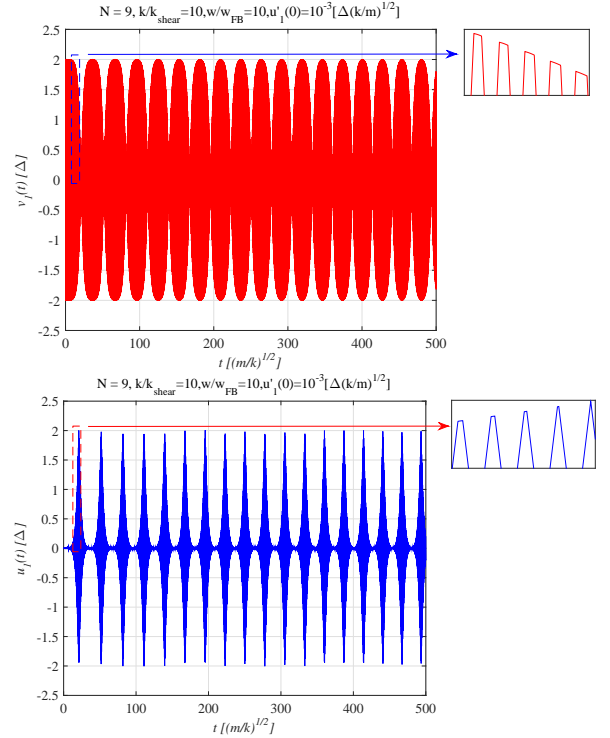


Fig. 12: Compacton integration results – 'PF' unstable case (principal-site histories)

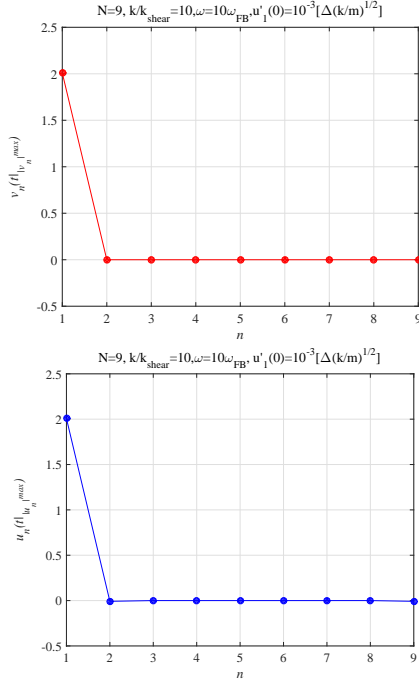


Fig. 13: Compacton integration results – ‘PF’ unstable case (maximum-amplitude profiles)

Moreover, the compacton mode is perfectly compact anyway for all frequencies. Consequently, for high frequencies, both modes are compact. Therefore, the entire dynamics is compact and is thus expected to be equivalent to the dynamics of a single element with high kinetic to potential energy ratios.

In [41], such an element is analyzed and global dynamics is revealed through transformation to canonic variables (action–angle formalism). One result arising in [41] is that the one-element cross-stitch system has a saddle point corresponding to the antisymmetric mode. This means that for high energies and finite stiffness-ratio values, the compacton solution should be unstable. Furthermore, the aforementioned saddle point is a global feature, and the nearest minimum corresponds to the symmetric mode. However, this does not yet imply that starting at the compacton initial conditions for high enough energies, one would stabilize the system in the symmetric mode. The reason is that, as shown in [41], there is no equal energy contour line passing through both the compacton-related saddle point and the breather-related minimum. Such stable global dynamic a route is hence inexistent.

What does exist is a contour line passing through the saddle point, reaching an intermediate location and going back to the saddle point. The intermediate location in the canonic phase-space is close enough to the symmetric mode. This dynamics correlates well-enough with the results of numerical integration of the chain given in Figs. 12-13.

## 5. Second model system (1D chain) – two-masses in a massless box, smooth internal potential, linear links

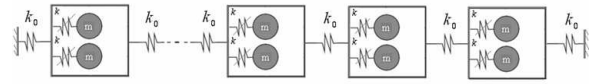


Fig. 14: Schematic picture of the second setting

Fig. 14 shows the second model-setting for the theoretical investigation performed in this paper.

For the required purposes, the interesting case would be that in which in every box the masses and spring stiffness constants are identical for the two oscillators (the reasoning is explained below). For such a case, the equations of motion for the system are as follows:

$$\begin{aligned} m\ddot{\bar{u}}_n + k(\bar{u}_n - u_n) &= f_{(\bar{u}_n - u_n)}^{NL} \\ m\ddot{\tilde{u}}_n + k(\tilde{u}_n - u_n) &= f_{(\tilde{u}_n - u_n)}^{NL} \end{aligned} \quad (46)$$

$$m\ddot{\bar{u}}_n + m\ddot{\tilde{u}}_n + k_0(2u_n - u_{n+1} - u_{n-1}) = 0$$

where  $\bar{u}_n$  and  $\tilde{u}_n$  denote the displacements of the first and the second oscillator, respectively, for each box, and  $u_n$  stands for the displacement of the  $n^{\text{th}}$  box itself. The conservative case (no external forcing and no damping) is assumed. The parameters  $k$  and  $k_0$  stand for spring rigidities inside and outside each box, respectively, and  $f_{(x)}^{NL}$  is interaction force derived from a smooth anharmonic correction to on-site potential, representing local material non-linearity.

### 5.1. Linear dynamics

The same set of equations can be written in normalized form, more convenient for mathematical treatment, which in the linear case becomes:

$$\begin{aligned} \ddot{\bar{u}}_n + \kappa(\bar{u}_n - u_n) &= 0 \\ \ddot{\tilde{u}}_n + \kappa(\tilde{u}_n - u_n) &= 0 \end{aligned} \quad (47)$$

$$\ddot{\bar{u}}_n + \ddot{\tilde{u}}_n + \gamma(2u_n - u_{n+1} - u_{n-1}) = 0$$

(here  $\kappa$  and  $\gamma$  stand for spring rigidities normalized by mass, inside and outside each box, respectively).

As in the previous model system, due to the symmetry between the first and second equations in 47, linear transformation of variables is employed, as follows:

$$v_n \triangleq \bar{u}_n - \tilde{u}_n, \quad x_n \triangleq \bar{u}_n + \tilde{u}_n \quad (48)$$

Combining 47 and 48, the following equivalent system of equations is obtained:

$$\begin{aligned} \ddot{v}_n + \kappa v_n &= 0 \\ \ddot{x}_n + \kappa x_n &= 2\kappa u_n \\ \ddot{x}_n + \gamma(2u_n - u_{n+1} - u_{n-1}) &= 0 \end{aligned} \quad (49)$$

The advantage of the employed transformation is evident, since the first equation in 49 decouples from the rest of the equations. Moreover, one observes that the first equation in 49 is a local relation, and indeed oscillatory spectral analysis results in a dispersion relation for  $v_n(t)$  that has the following form:

$$\omega_0(q) = \sqrt{\kappa} \quad (50)$$

in which  $\omega_0$  stands for the frequency and  $q$  denotes the wavenumber. Once again, due to local configurational symmetry, a flat band emerges.

Next, proceeding to the two remaining equations in system 49, one finds that a plane wave oscillatory solution of this system is only possible in the case of synchronous motion of  $u_n$  and  $x_n$  (which is reasonable, since oscillatory motion requires mass inertia which is supplied to  $u_n$  by  $x_n$ ). For such motion, the corresponding dispersion relation takes the form:

$$\hat{\omega}_1(q) = \sqrt{\frac{1 - \cos q}{1 - \cos q + \delta}} \quad (51)$$

where  $\delta \triangleq \kappa/\gamma$  and  $\omega_1 = \sqrt{\kappa}\hat{\omega}_1 < \omega_0$  (implying no-crossing, unlike in [37]),  $\omega_1$  being the frequency. One can observe that in the limit  $\delta \gg 1$ , the dispersion relation of a simple linear chain is recovered, whereas in the limit  $\delta \ll 1$ , this dispersion relation becomes (asymptotically) flat as well.

Another simple linear mechanical system that has a flat band structure has therefore been demonstrated. To conclude this part of the description, plot of the oscillatory spectra of the system is presented below, illustrating the flat band in more detail (Fig. 15).

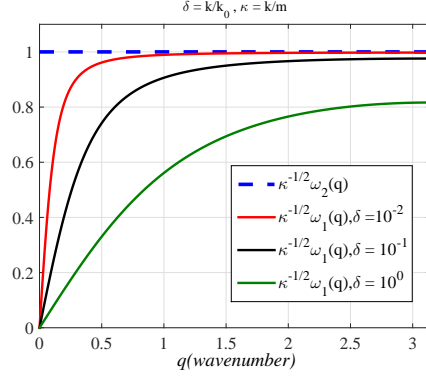


Fig. 15: Dispersion relations (flat band in dash)

## 5.2. Nonlinear dynamics: single element analysis

The basic system subjected to nonlinear analysis is represented by Fig. 16.

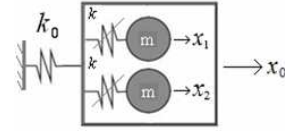


Fig. 16: Schematic picture of a representative element for nonlinear analysis

In line with the well-known Fermi-Pasta-Ulam theory, cubic nonlinearity is added to the internal interaction forces, producing the following equations of motion:

$$\begin{aligned} m\ddot{x}_1 + k(x_1 - x_0) + p(x_1 - x_0)^3 &= 0 \\ m\ddot{x}_2 + k(x_2 - x_0) + p(x_2 - x_0)^3 &= 0 \\ k_0x_0 - k(x_1 - x_0) - p(x_1 - x_0)^3 \\ -k(x_2 - x_0) - p(x_2 - x_0)^3 &= 0 \end{aligned} \quad (52)$$

Since the conservative case is considered, with no forcing or damping, the general expression for the energy of the model system is given by:

$$\begin{aligned} E = E_0 &= \frac{1}{2}m\dot{x}_1^2 + \frac{1}{2}m\dot{x}_2^2 + \frac{1}{2}k_0x_0^2 \\ &+ \frac{1}{2}k(x_1 - x_0)^2 + \frac{1}{4}p(x_1 - x_0)^4 \\ &+ \frac{1}{2}k(x_2 - x_0)^2 + \frac{1}{4}p(x_2 - x_0)^4 \end{aligned} \quad (53)$$

Next, appropriate notation is introduced:

$$\bar{x} \triangleq \frac{x_1 + x_2}{2}, \quad v \triangleq x_1 - x_2, \quad y \triangleq \bar{x} - x_0, \quad \tilde{p} \triangleq \frac{p}{2k} \quad (54)$$

$$C \triangleq 4\hat{\eta}\hat{\epsilon}^2 + (1 + 4\hat{\eta})\hat{\epsilon} + 1 + \hat{\eta} \quad (55)$$

where the auxiliary quantities are given by:

$$\omega = \sqrt{k/m}, \quad \hat{\eta} \triangleq 2k/k_0, \quad \hat{\epsilon} \triangleq \tilde{p}Y_0^2 \quad (56)$$

This can be used to derive the relation between energy and symmetric-mode amplitude,  $Y_0$  (later used, for convenience, in parametric analysis):

$$\frac{E_0}{k} = (1 + \hat{\eta})Y_0^2 + (1 + 4\hat{\eta})\tilde{p}Y_0^4 + 4\hat{\eta}\tilde{p}^2Y_0^6 \quad (57)$$

The antisymmetric mode corresponds to zero motion of the center-of-mass of the system, which leads, following the definitions in Eq. (54), to the following relations:

$$\bar{x}(t) \equiv 0 \stackrel{(52,54)}{\Rightarrow} x_0(t), y(t) \equiv 0, x_{1,2} = \pm v/2 \quad (58)$$

Taking the difference of the first two equations in Eqs. (52), expressed in terms of  $y, v$  and  $x_0$ , after eliminating  $x_0$  using the third, algebraic equation in Eqs. (52), and its first and second time derivatives, expressed in terms of the three aforementioned variables, leads to the following equation:

$$\ddot{v} + \omega^2(1 + 6\tilde{p}y^2)v + \frac{1}{2}\tilde{p}\omega^2v^3 = 0 \quad (59)$$

Substituting Eq. 58 into the expression for the total energy of the system given in Eq. (53), and using Eqs. (54) and (56)-(57), one obtains the first integral of the antisymmetric mode of the system, in the following form:

$$[\hat{v}']^2 + \hat{v}^2 + \frac{1}{4}\hat{\epsilon}\hat{v}^4 = 4C; \quad \hat{v} \triangleq v/Y_0, \quad (60)$$

$$\hat{v}' \triangleq d\hat{v}/d\tau, \quad \tau \triangleq \omega t$$

(here  $Y_0(E_0, k_0, k, p)$  is perceived merely as convenient parametrization of the total energy in the system).

Further integration of Eq. 60 results in a closed form expression for the normalized antisymmetric mode displacement as a function of the dimensionless time, using the fifth Jacobi elliptic function 'sd', as follows:

$$\hat{v}(\tau) = \frac{\sqrt{4C}\text{sd}\left[(1 + 4\hat{\epsilon}C)^{1/4}\tau \left| \frac{\sqrt{1+4\hat{\epsilon}C}-1}{2\sqrt{1+4\hat{\epsilon}C}} \right. \right]}{(1 + 4\hat{\epsilon}C)^{1/4}} \quad (61)$$

One observes that for small amplitudes, the simple form  $\hat{v}(t) = \sin(\omega t)$  is reproduced.

Eq. (61) provides the explicit solution for the antisymmetric mode. In order to study its stability, Floquet-Hill strategy is followed, and Fourier-series representation of the solution is called for. The sine series representation of  $\text{sd}(z|m)$  is presented in [42]. In the employed parametrization it gives rise to the following series for the antisymmetric mode:

$$\hat{v}(\hat{\tau}) = \sum_{n=1}^{\infty} V_n \sin(n\hat{\tau}), \quad \hat{\tau} \triangleq \Omega_v \tau \quad (62)$$

where

$$\hat{m} \triangleq \frac{\sqrt{1 + 4\hat{\epsilon}C} - 1}{2\sqrt{1 + 4\hat{\epsilon}C}}, \quad \Omega_v \triangleq \frac{\pi(1 + 4\hat{\epsilon}C)^{1/4}}{2K(\hat{m})},$$

$$V_n \triangleq \frac{2\pi\sqrt{C}(1 + 4\hat{\epsilon}C)^{-1/4}}{\sqrt{\hat{m}(1 - \hat{m})}K(\hat{m})} \frac{(-1)^{\frac{n-1}{2}}\delta_{n,2\mathbb{N}-1}}{\cosh\left[\frac{n\pi K(1-\hat{m})}{2K(\hat{m})}\right]} \quad (63)$$

and  $K(m)$  is the complete elliptic integral of the first kind (and  $\delta_{a,b}$  is Kronecker's delta).

### 5.2.1. Derivation of the Hill equation

In order to examine the linear stability of the obtained solution, the equation of motion for the symmetric mode is required.

Finding from Definition (54) that:

$$x_{1,2} - x_0 = y \pm v/2 \quad (64)$$

and substituting this in the third equation in Eqs. (52), one obtains the equation of motion for the displacement of the box, as follows:

$$x_0 = y \left( \hat{\eta} + 2\hat{\eta}\tilde{p}y^2 + \frac{3}{2}\hat{\eta}\tilde{p}v^2 \right) \quad (65)$$

Next, taking half of the sum of the first two equations in Eqs. (52) and substituting Eq. (64), the third of Definitions (54) and the second time derivative of Eq. (65) into the result, eliminating the second time derivative of  $v$  by isolating it from Eq. (59), one obtains the equation of motion for the symmetric mode for the case of full dynamics, containing only  $v, y$ , their first time derivatives and the second time derivative of  $y$ , in terms of the dimensionless quantities defined in Eq. 62 and in the first row in Eq. (63). Next, linearizing with respect to  $y(t)$ , one obtains the equation for linear perturbations to the antisymmetric mode. Additional mathematical manipulations, described in [35], produce the explicit Hill form of the linear stability equation for the purely antisymmetric mode:

$$\tilde{y}''(\hat{\tau}) + \frac{\Omega_v^{-2}}{1 + \hat{\eta}} \frac{1 + (3/2)\hat{\epsilon}[\hat{v}(\hat{\tau})]^2}{1 + (3/2)\frac{\hat{\eta}}{1+\hat{\eta}}\hat{\epsilon}[\hat{v}(\hat{\tau})]^2} \tilde{y}(\hat{\tau}) = 0 \quad (66)$$

with  $\Omega_v$  and  $\hat{v}(\hat{\tau})$  given by Eqs. (62)-(63), and with the Hill function,  $h(\hat{\tau})$ , being the expression multiplying  $\tilde{y}(\hat{\tau})$  in Eq. (66).

In the next subsection, numerical Floquet analysis of Eq. (66) is performed using rigorous deconvolution and application of Hill's method, for identification of instability tongues characterizing the antisymmetric mode. Asymptotic analysis of Eq. (66), resulting in the identification of the number of emerging instability tongues, derivation of starting points at the zero-amplitude limit for numerical instability-tongue boundaries calculation, as well as leading-order asymptotic expansions for the boundaries of the first two instability tongues, using both Mathieu and higher-order approximations, appears in [35].

### 5.2.2. Floquet analysis of the Hill equation (Fourier decomposition by numerical deconvolution)

In order to perform stability analysis by Hill's Determinants Method, the Hill function in Eq. (66) has to be expressed as a Fourier series. To this end, first, the numerator and the denominator are decomposed, separately. Both the numerator and the denominator depend linearly on the square of the normalized displacement in the antisymmetric mode,  $\hat{v}(\hat{\tau})$ , which was already expressed in a sine series form (Eq. (62)). Thus the first thing one has to do is to perform convolution, since the Fourier series decomposition of the product of two functions (a function and itself, in the present case) equals the (discrete) convolution of the Fourier series decomposition of each of the functions. Multiplying, rearranging and adjusting the indices, one obtains the following expression:

$$[\hat{v}(\hat{\tau})]^2 = \frac{V_0^{(2)}}{2} + \sum_{k=1}^{\infty} V_k^{(2)} \cos(2k\hat{\tau}),$$

$$V_k^{(2)} \triangleq \left[ \sum_{m=1,3,5}^{\infty} V_m V_{2k+m} - \frac{1}{2} V_k^2 \delta_{k,2\mathbb{N}-1} \right. \\ \left. - (1 - \delta_{k,1}) \sum_{m=1}^{\infty} V_{k-m} V_{k+m} \right] \delta_{k,\mathbb{N}-1} \quad (67)$$

Next the definition of the Hill function, as arising from Eq. (66), is rearranged to a product form,  $f_1(\hat{\tau})h(\hat{\tau}) = f_2(\hat{\tau})$ , and then  $h(\hat{\tau})$  is formally expanded into a Fourier cosine series (as the ratio of two even functions,  $h(\hat{\tau})$  is always even):

$$h(\hat{\tau}) = \frac{H_0}{2} + \sum_{k=1}^{\infty} H_k \cos(2k\hat{\tau}) \quad (68)$$

Substituting Eqs. (67) and (68) into the aforementioned product-form equation for  $h(\hat{\tau})$  that emerges from Eq. (66), expanding the resulting products of sums, using trigonometric identities to turn cosine products to single index-shifted cosines and performing the convolution, one finally obtains the product-form equation for  $h(\hat{\tau})$  as a single Fourier cosine series that should be equal to zero at all times, namely,  $g(\hat{\tau}) = G_0 + \sum_{n=1}^{\infty} G_n \cos(2n\hat{\tau}) \equiv 0$ .

Fulfillment of this condition corresponds to the vanishing of the coefficients of this Fourier series. The equations representing the vanishing of these *total* Fourier cosine series coefficients, formulated as equations for the Fourier cosine coefficients of  $h(\hat{\tau})$ , take the form of linear algebraic equations.

First, there is the condition  $G_0 = 0$ , producing the following explicit equation for  $H_0$  in terms of  $H_{n \geq 1}$ :

$$H_0 = \frac{\Omega_v^{-2}(4 + 3\hat{\epsilon}V_0^{(2)})}{2(1 + \hat{\eta}) + (3/2)\hat{\eta}\hat{\epsilon}V_0^{(2)}} - \frac{3\hat{\eta}\hat{\epsilon}}{2(1 + \hat{\eta}) + (3/2)\hat{\eta}\hat{\epsilon}V_0^{(2)}} \sum_{n=1}^{\infty} V_n^{(2)} H_n \quad (69)$$

Second, taking the set of conditions  $G_{n \geq 1} = 0$ , which contain both  $H_0$  and  $H_{n \geq 1}$ , and eliminating  $H_0$  from these equations by isolating it from Eq. (69), one obtains an infinite set of linear inhomogeneous equations for  $H_{n \geq 1}$ , which takes the following form in indicial notation:

$$\sum_{m=1}^{\infty} M_{nm} H_m = \mu_n \quad ; \quad \forall \quad n, m \in \mathbb{N}$$

$$\mu_n = \frac{3\hat{\epsilon}\Omega_v^{-2}\delta_{n,\mathbb{N}}V_n^{(2)}}{2 + 2\hat{\eta} + (3/2)\hat{\eta}\hat{\epsilon}V_0^{(2)}}$$

$$M_{nm} = \left( 1 + \hat{\eta} + \frac{3}{4}\hat{\eta}\hat{\epsilon}V_0^{(2)} \right) \delta_{n,m} \quad (70)$$

$$+ \frac{3}{4}\hat{\eta}\hat{\epsilon}V_{n+m}^{(2)}\delta_{n+m,\mathbb{N}} + \frac{3}{4}\hat{\eta}\hat{\epsilon}V_{n-m}^{(2)}\delta_{n-2m,\mathbb{N}}$$

$$+ \frac{3}{4}\hat{\eta}\hat{\epsilon}V_{m-n}^{(2)}\delta_{m-n,\mathbb{N}} + \frac{3}{4}\hat{\eta}\hat{\epsilon}V_m^{(2)}\delta_{n,2m}$$

$$- \frac{3}{4}\hat{\eta}\hat{\epsilon} \frac{3\hat{\eta}\hat{\epsilon}V_n^{(2)}V_m^{(2)}}{2 + 2\hat{\eta} + (3/2)\hat{\eta}\hat{\epsilon}V_0^{(2)}}$$

Finally, Eqs. (70) are truncated, exchanging  $\mathbb{N}$  by  $\mathbb{N} \leq \hat{N}$  everywhere in these equations (this is the reason for the presence of Kronecker's delta in the first term in the third row in Eq. (70)), and deconvolution is performed by solving the truncated

system numerically, by a standard algorithm for the solution of linear systems, thus producing  $H_{n \geq 1}$ . Coefficient  $H_0$  is then derived using Eq. (69).

The issue of convergence for this procedure is discussed in [35]. Having obtained the Fourier cosine coefficients of the Hill function, one performs the stability analysis by Hill's (truncated) Infinite Determinants method. The result is shown in Fig. 17.

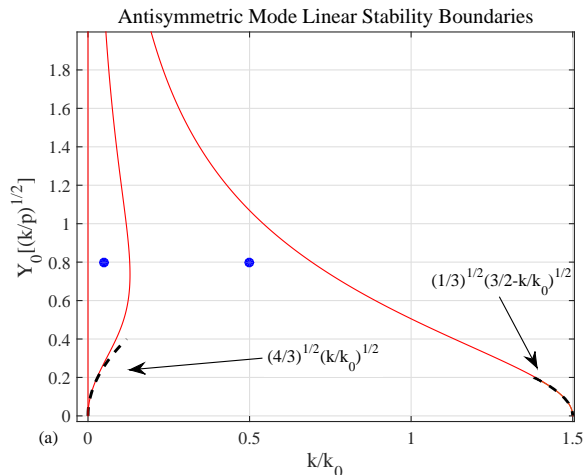


Fig. 17: Linear stability bounds in solid with asymptotic estimates in dash and the two points chosen for numerical integration

### 5.2.3. Asymptotic stability-limit estimates

The small-amplitude (given for energy in amplitude units, following Eq. (57)) analytic estimates for the stability boundaries, as derived in [35] are:

$$\begin{aligned} \frac{k}{k_0} \Big|_{-}^{(1)} \xrightarrow{Y_0 \rightarrow 0} 0, \quad Y_0 \Big|_{+}^{(1)} \xrightarrow{k/k_0 \rightarrow 0} \sqrt{\frac{4}{3}} \sqrt{\frac{k}{k_0}}, \\ Y_0 \Big|_{\pm}^{(2)} \xrightarrow{k/k_0 \rightarrow 0} \sqrt{\frac{1}{3}} \sqrt{\frac{3}{2} - \frac{k}{k_0}} \end{aligned} \quad (71)$$

Plots of the first (finite-width) instability tongue boundaries for the antisymmetric mode, and the second tongue, which is (at least to second order) a collapsed, zero-width one, are presented in Fig. 17. Asymptotic approximations for the boundaries, as given in Eq. 71, are shown therein in dash.

Figs. 18-19 present Poincaré sections of the flow in the vicinity of the second (degenerate) instability tongue. The emergence of KAM islands represents the effect of the loss of stability of the compact mode through parametric resonance.

The coordinates in the plots are the symmetric mode displacement and normalized time derivative. Hence, energy localized entirely in the compact, antisymmetric mode is represented as a point in the center (or an oval around the center, in the perturbed case). As stability is lost, the oval around the center turns into four KAM islands, corresponding to the 1:2 resonance of the second tongue.

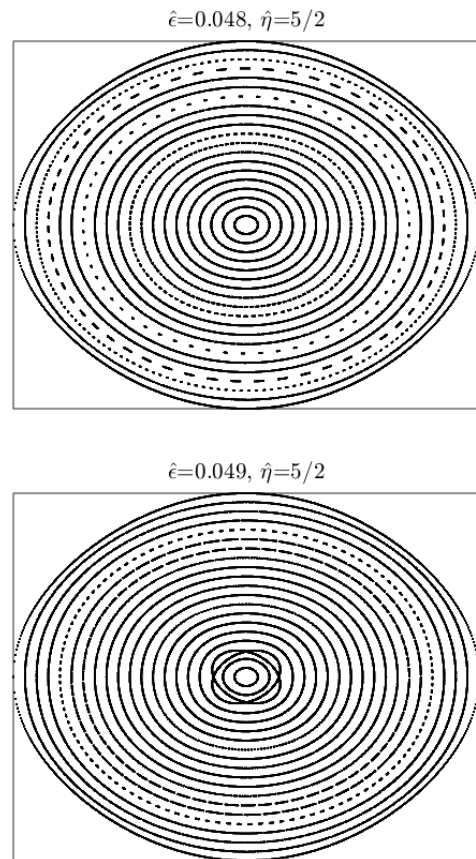


Fig. 18: Poincaré sections in (normalized) symmetric mode displacement and velocity for energy just below and above the degenerate instability tongue

The single-element analysis presented here is reproduced in part from [35], for better understanding of the dynamics in the context of a chain. This owes to the fact that for a chain, rigorous stability analysis is not within reach, other than when understanding the single element case as representative of the anti-continuum limit for a chain, taking  $k/k_0 \gg 1$ . In that limit, as Fig. 17 shows, the compacton is linearly stable (see [35] for proof).

## 6. Numerical integration for a chain

The stability of a compacton in the chain shown in Fig. 14 can be examined by taking parameters inside and outside of the finite-width instability tongue, as calculated for a single element. This embodies the (verifiable) assumption that the stability limits for a chain are somehow correlated with those of a single element. The two points in the stiffness-ratio – energy plane chosen for stability analysis by direct integration of a chain are shown in Fig. 17. In order to perform the numerical integration from the perspective of stability of (nonlinear) normal modes (NNMs), first, the equations of motion given in Eq. 46 for the case of cubic nonlinearity in the internal interaction forces, are rewritten as a dynamic system in which modal displacements can be integrated directly.

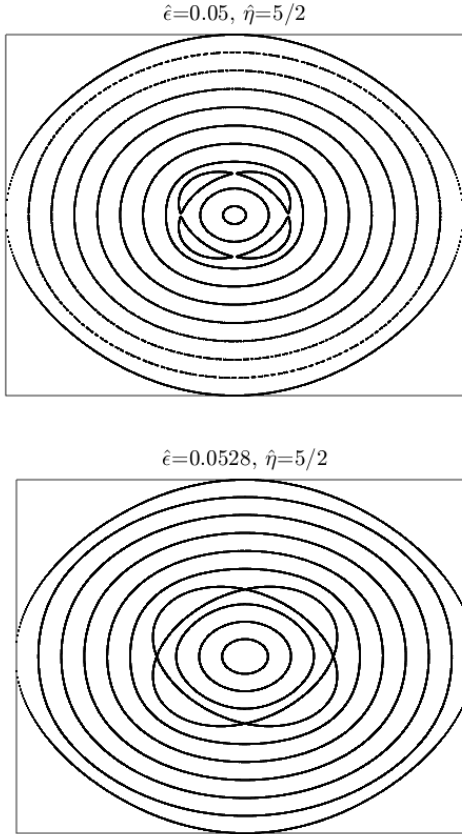


Fig. 19: Poincaré sections, illustrating the effect of the degenerate instability tongue on the topology, for energies further above the critical line. KAM islands emanate from the compact mode as energy is increased

### 6.1. Equations of motion

The equations of motion for a chain of  $N$  elements containing massless boxes, occupied by two identical internal oscillators with linear-cubic interaction with the box are given below. The equations are expressed in terms of the dimensionless quantities,  $\hat{v}_i, \hat{y}_i$ , representing the displacement difference of the internal oscillators and the center of mass displacement with respect to the box.

$$\hat{v}_i'' = -(1 + 6\hat{\epsilon}\hat{y}_i^2)\hat{v}_i - 2\hat{\epsilon}\hat{v}_i^3, \quad \hat{y}_i'' = -\hat{M}_{ij}\hat{f}_j \quad (72)$$

$$\hat{\mathbf{M}} \triangleq \mathbf{M}^{-1}, \quad \hat{\mathbf{B}} \triangleq \mathbf{B}^{-1}, \quad \hat{\mathbf{Q}} \triangleq \hat{\mathbf{B}}\mathbf{Q} \quad (73)$$

$$\hat{\mathbf{f}} \triangleq \hat{\mathbf{y}} + 2\hat{\epsilon}\boldsymbol{\mu} + 24\hat{\epsilon}\hat{\mathbf{B}}(\boldsymbol{\phi} - \boldsymbol{\lambda})$$

$$M_{ij} \triangleq \delta_{ij} + 2\hat{B}_{ij} + 12\hat{\epsilon}\hat{Q}_{ij}$$

$$B_{ij} \triangleq \eta\delta_{ij} - \frac{\eta}{2}(\delta_{i+1,j} + \delta_{i,j+1}) \forall i, j \in \mathbb{N} < N$$

$$B_{NN} = \eta, \quad Q_{ij} \triangleq (\hat{y}_i^2 + \hat{v}_i^2)\delta_{ij} \quad (74)$$

$$\phi_i \triangleq \hat{y}_i(\hat{y}_i')^2 + 2\hat{v}_i\hat{y}_i'\hat{v}_i' + \hat{y}_i(\hat{v}_i')^2$$

$$\mu_i \triangleq \hat{y}_i^3 + 3\hat{y}_i\hat{v}_i^2, \quad \lambda_i \triangleq \hat{y}_i\hat{v}_i^2[1 + 2\hat{\epsilon}(\hat{v}_i^2 + 3\hat{y}_i^2)]$$

In order to avoid singularity, the system described by the matrix given in Eq. 74 is statically condensed by one degree of freedom related to rigid-body motion. In addition, in order to avoid boundary effects, the chain is closed into a ring, providing the spatially extended dynamical system given above with periodic boundary conditions.

### 6.2. Integration results

*Unstable case (moderate amplitude).* The first result is obtained by taking the left point in Fig. 17, the one lying well within the instability tongue for a single element. The initial condition is a slightly perturbed compacton solution. A stable integration algorithm with a bounded energy error is employed. It appears, as shown in Fig. 20, that the stability of the compacton solution is lost, and small, yet finite-amplitude, center-of-mass relative (to the boxes) displacements emerge for the ringed chain.

Fig. 20 illustrates the instability of the identical zero solution for the symmetric mode, as emerging from a slight perturbation. The packets-pattern is typical for energy exchange between different NNMs, by the mechanism of parametric resonance (at least initially in the process of loss of stability). This energy exchange between modes is similar to what can be observed on a Poincaré section for a single element (see [35]).

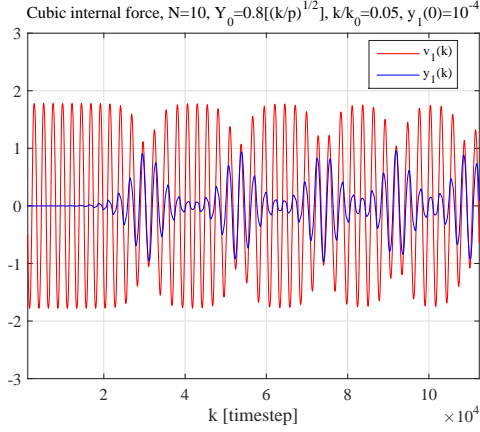


Fig. 20: Unstable case – initial emergence of instability, as illustrated by the dynamics of the principal element in the chain (the compacton site)

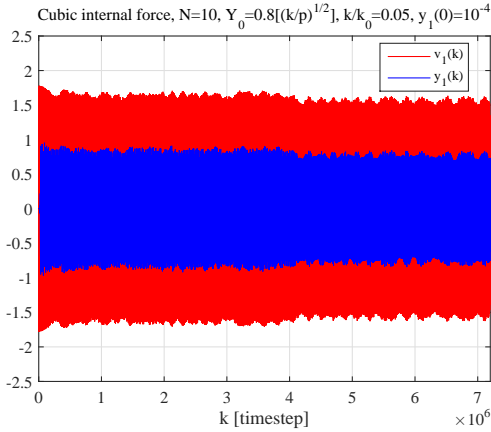


Fig. 21: Unstable case – long-time history

Fig. 21 shows the long-time history after all transients are gone. One observe significant energy exchange following the local instability of the compacton (zero symmetric mode) solution.

Fig. 22 shows the flow close to a global bifurcation where KAM islands of the symmetric and antisymmetric modes "collide", corresponding to the aforementioned significant (1:2 resonance for both modes) energy exchange (see [35]).

Fig. 23 shows the envelope of the symmetric mode displacement of the chain, which has the typical profile of a breather, with partial localization arising from the (cubic) on-site nonlinearity.

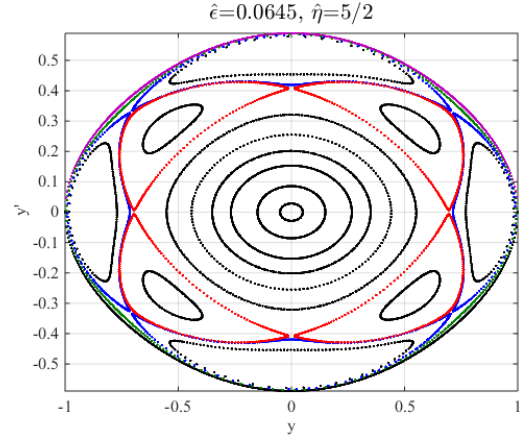


Fig. 22: Poincaré section: global-bifurcation dynamics

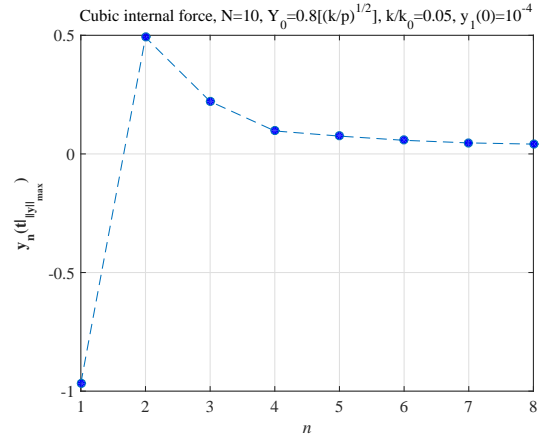


Fig. 23: Unstable case: breather mode profile

*Stable case (moderate amplitude).* The second result is obtained when taking the rightmost point in Fig. 17, the one lying well inside the stable region for a compacton in a representative element. Integration is carried out starting from a slightly perturbed compacton initial condition.

Fig. 24 shows that when starting from the same perturbation to the compacton as in the unstable-parameters' case, the perturbation stays bounded, i.e. there is no delocalization. This is illustrated by the maximum-amplitude profile of the symmetric mode displacement and the antisymmetric mode displacement history, which exhibits stable periodic dynamics.

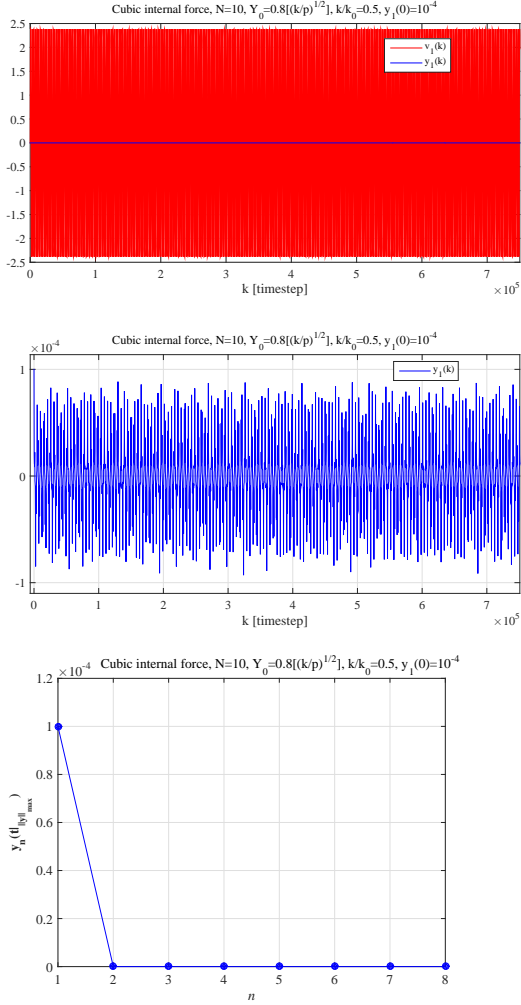


Fig. 24: Integrations results – stable case (top to bottom): antisymmetric mode displacement history, symmetric mode displacement history and maximum amplitude symmetric mode profile

Figs. 21-24 show that as predicted by linear stability analysis for a representative element, the non-linearity may either retain or destroy the stability of the compacton solution. The sheer existence of the compacton is, of course, emerging from the configurational symmetry corresponding to the existence of a flat band in the dispersion spectrum of the system. It also appears that the periodic dynamics in a ring can correspond to a combination of a perfectly compact mode, namely the compacton, emerging due to configurational symmetry, and a partially localized mode, namely a breather mode, corresponding to localization-inducing on-site non-

linearity.

The following subsection extends the analysis to the case of a high-amplitude (high energy) regime, where additional noteworthy phenomena are observed.

### 6.2.1. High-amplitude regime – unstable case

The next result is obtained by increasing the (dimensionless) amplitude one order of magnitude and finding a corresponding stiffness ratio for which the representative element analysis shows the compacton solution to be unstable. This appears to correspond to highly rigid inter-site link potential, and repeating the integration, the obtained results remind those presented in Figs. 21-23. There appears to be the additional property that the breather solution possesses a higher level of spatial localization, which can be attributed to the higher energy contained in the system. This matter is elaborated on in the analysis in the final subsection in this paper.

Fig. 25 shows the principal site antisymmetric mode displacement history for the perturbed case on top of the result for the unperturbed case. The results exhibit, once again, the energy exchange feature representative of parametric resonance of the compacton with the symmetric mode. Fig. 26 shows the symmetric mode displacement's first energy packet history, and the maximum amplitude symmetric mode displacement profile. One notes that the extent of energy exchange for the high-energy regime is almost maximal – considerably higher than the partial energy exchange observed in the moderate amplitude regime

The following subsection exhibits the integration results in the high-amplitude regime corresponding to a stiffness ratio well inside the stable region for the representative element analysis.

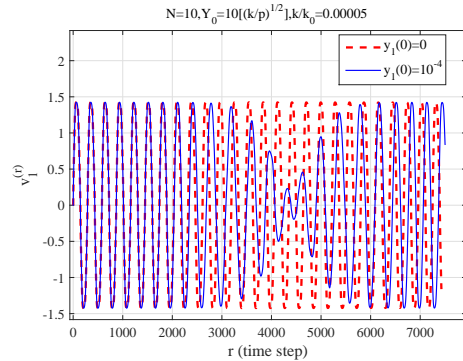


Fig. 25:  $v_1(t)$  – high amplitude (unstable)

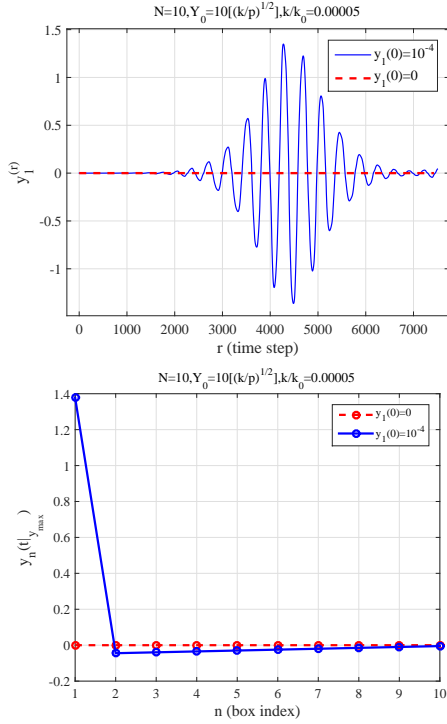


Fig. 26:  $y_1(t), y_n^{max}$  – high amplitude (unstable)

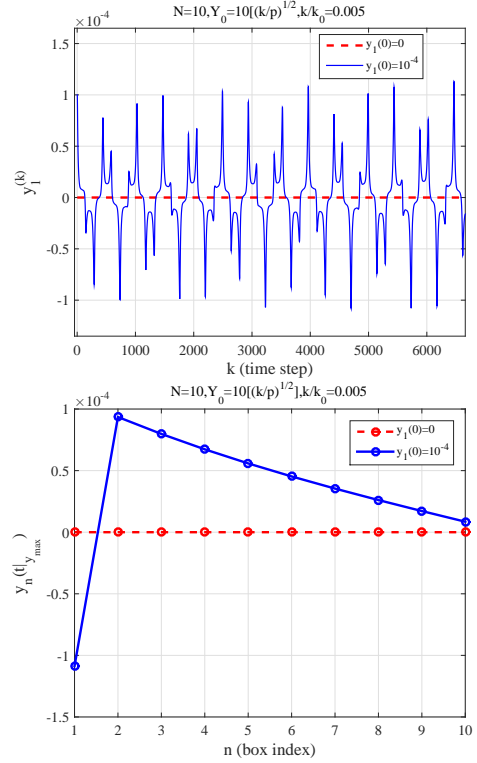


Fig. 28:  $y_1(t), y_n^{max}$  – high amplitude (stable)

### 6.2.2. High-amplitude regime – stable case

Figs. 27-28 show integration results for the slightly perturbed compacton conditions (in blue online) on top of the unperturbed ones. The stability of the compacton is evident.

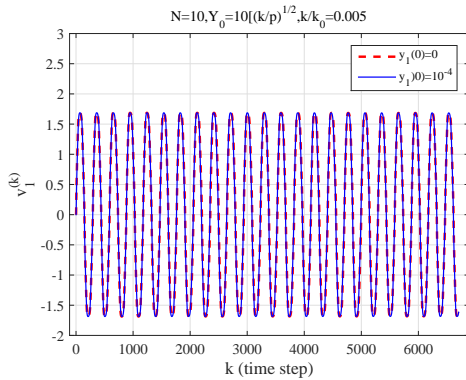


Fig. 27:  $v_1(t)$  – high amplitude (stable)

## 7. Conclusions

In this paper two 1D discrete mechanical nonlinear lattices were examined that are characterized by having flat dispersion bands. It was established that originating from the flat bands, the systems possess perfectly compact linearly stable periodic solutions.

For the non-smooth system, the compacton solution as well as its counterpart, the breather solution, were derived analytically for a finite chain. Moreover, their linear stability was examined rigorously, using the experience in non-smooth stability analysis gained by study of DBs, as in [11]. In particular, asymptotic estimates for stability bounds in the parameter space were derived. The stability analysis was validated by direct numerical integration.

For the smooth system, the compact solution was derived analytically and rigorous stability analysis was performed for a representative element. The obtained result has evident implications for a chain in the anti-continuum limit (which are –

all compactons in this limit are stable). Consequently, the stability of the solution in an actual chain was established numerically for parameters in the range relevant for the prediction made by the representative-element analysis.

Some light was shed on the global dynamics for each of the systems, borrowing from the results given in [35] and [41].

To put the mathematical perspective aside, a perfectly compact periodic solution, having a finite stability range, may be relevant for such engineering applications as sensing/actuating or switching, especially if lattice engineering as in [33] is considered, but with application of rigorous stability analysis tools. This may comprise future work on the subject.

## Acknowledgments

The authors are grateful to the Israel Science Foundation (grant 838/13) for financial support.

## Appendix A. Derivation of the saltation matrix for asynchronous two-impact jumps

*First impact.* For the first impact, the following relations hold, assuming small impact time (which owes to impact idealization) and small solution perturbation (pertinent to linear stability analysis):

$$\begin{aligned}
\bar{\mathbf{x}}(\bar{T}_-) &= \mathbf{x}(\bar{T}_-) + \delta\mathbf{x}_- \\
\bar{\mathbf{x}}(T_-) &= \bar{\mathbf{x}}(\bar{T}_+) + \mathbf{A}\bar{\mathbf{x}}(\bar{T}_+)\delta t \\
\bar{\mathbf{x}}(\bar{T}_+) &= \mathbf{g}_1[\bar{\mathbf{x}}(\bar{T}_-), \bar{T}_-] \\
\bar{\mathbf{x}}(T_+) &= \mathbf{x}(T_+) + \delta\mathbf{x}_+ \\
\mathbf{x}(T_-) &= \mathbf{x}(\bar{T}_+) + \mathbf{A}\mathbf{x}(\bar{T}_+)\delta t \\
\mathbf{x}(T_+) &= \mathbf{g}[\mathbf{x}(T_-), T_-] \\
\bar{\mathbf{x}}(T_-) &= \bar{\mathbf{x}}(T_+) \\
\mathbf{x}(\bar{T}_-) &= \mathbf{x}(\bar{T}_+)
\end{aligned} \tag{A.1}$$

where the smooth dynamics is linear and is represented by:  $\dot{\mathbf{x}} = \mathbf{A}\mathbf{x}$ , jump corresponding to a single mass impact is represented by the mapping  $\mathbf{g}_1(\mathbf{x}, t)$ , jump corresponding to impact of two masses at a two-mass site is represented by the mapping  $\mathbf{g}(\mathbf{x}, t)$ , the periodic solution is  $\mathbf{x}$ , the perturbed solution is  $\bar{\mathbf{x}}$ , the perturbation in the solution is  $\delta\mathbf{x}$ , the impact instance of the unperturbed solution is  $T$ , the *first*-impact instance of the perturbed solution is  $\bar{T}$ , and it is assumed (with no loss of generality) that one

has  $T > \bar{T}$ , and the subscripts '+' and '-' denote limit-values before and after impacts.

Combining the eight equations in Eqs. A.1, and expanding the mappings  $\mathbf{g}_1$  and  $\mathbf{g}$  as first order multiple-variable Taylor series (which is justified for the rather general case of a smooth mapping representing impact), and retaining only first-order terms, the following relation is obtained:

$$\begin{aligned}
\delta\mathbf{x}_+ &= \mathbf{g}_1[\mathbf{x}(T_-), T_-] - \mathbf{g}[\mathbf{x}(T_-), T_-] + \\
&+ \{\nabla\mathbf{g}_1^\top[\mathbf{x}(T_-), T_-]\}^\top \delta\mathbf{x}_- + \left( \mathbf{A}\mathbf{g}_1[\mathbf{x}(T_-), T_-] \right. \\
&\left. - \{\nabla\mathbf{g}_1^\top[\mathbf{x}(T_-), T_-]\}^\top \mathbf{A}\mathbf{x}(T_-) + \frac{\partial\mathbf{g}_1[\mathbf{x}(T_-), T_-]}{\partial t} \right) \delta t
\end{aligned} \tag{A.2}$$

where  $\delta t = T - \bar{T}$  is obtained as a function of  $\delta\mathbf{x}_-$  by use of the jump conditions, as follows. The jump conditions for the periodic and perturbed solution as related to the first impact are given by:

$$\begin{aligned}
h_1[\mathbf{x}(T_-), T_-] &= 0 \\
h_1[\bar{\mathbf{x}}(\bar{T}_-), \bar{T}_-] &= 0
\end{aligned} \tag{A.3}$$

Substituting Eqs. A.1(e), A.1(h) and A.1(a) into Eq. A.3(b), performing a first-order Taylor series expansion, and employing Eq. A.3(a), one obtains an equation relating  $\delta t$  and  $\delta\mathbf{x}_-$ , which reads:

$$\delta t = \frac{\{\nabla^\top h_1[\mathbf{x}(T_-), T_-]\} \delta\mathbf{x}_-}{\{\nabla^\top h_1[\mathbf{x}(T_-), T_-]\} \mathbf{A}\mathbf{x}(T_-) - \frac{\partial h_1[\mathbf{x}(T_-), T_-]}{\partial t}} \tag{A.4}$$

Substituting Eq. A.4 into Eq. A.2, one obtains the following relations:

$$\delta\mathbf{x}_+ = \mathbf{g}_1[\mathbf{x}(T_-), T_-] - \mathbf{g}[\mathbf{x}(T_-), T_-] + \mathbf{S}_1 \delta\mathbf{x}_- \tag{A.5}$$

$$\begin{aligned}
\mathbf{S}_1 &\triangleq \{\nabla\mathbf{g}_1^\top[\mathbf{x}(T_-), T_-]\}^\top + \left( \mathbf{A}\mathbf{g}_1[\mathbf{x}(T_-), T_-] \right. \\
&\left. - \{\nabla\mathbf{g}_1^\top[\mathbf{x}(T_-), T_-]\}^\top \mathbf{A}\mathbf{x}(T_-) + \frac{\partial\mathbf{g}_1[\mathbf{x}(T_-), T_-]}{\partial t} \right) \\
&\times \frac{\nabla^\top h_1[\mathbf{x}(T_-), T_-]}{\{\nabla^\top h_1[\mathbf{x}(T_-), T_-]\} \mathbf{A}\mathbf{x}(T_-) - \frac{\partial h_1[\mathbf{x}(T_-), T_-]}{\partial t}}
\end{aligned} \tag{A.6}$$

*Second impact.* For the second impact, the fol-

lowing relations hold:

$$\begin{aligned}
\bar{\mathbf{x}}(T_+) &= \mathbf{x}(T_+) + \delta\mathbf{x}_+ \\
\bar{\mathbf{x}}(\hat{T}_-) &= \bar{\mathbf{x}}(T_+) + \mathbf{A}\bar{\mathbf{x}}(T_+)\delta\bar{t} \\
\bar{\mathbf{x}}(\hat{T}_+) &= \mathbf{g}_2[\bar{\mathbf{x}}(\hat{T}_-), \hat{T}_-] \\
\bar{\mathbf{x}}(\hat{T}_+) &= \mathbf{x}(\hat{T}_+) + \delta\mathbf{x}_{++} \\
\mathbf{x}(\hat{T}_-) &= \mathbf{x}(T_+) + \mathbf{A}\mathbf{x}(T_+)\delta\bar{t} \\
\mathbf{x}(\hat{T}_+) &= \mathbf{x}(\hat{T}_-)
\end{aligned} \tag{A.7}$$

where the jump corresponding to the second mass impact (for the perturbed periodic solution) is represented by the mapping  $\mathbf{g}_2(\mathbf{x}, t)$ , the perturbation in the solution after both impacts occurred in both the perturbed and unperturbed solution is  $\delta\mathbf{x}_{++}$ , the *second*-impact instance of the perturbed solution is  $\hat{T}$ , and one has  $\delta\bar{t} = \hat{T} - T > 0$ .

Combining the six equations in Eqs. A.7, expanding the mapping  $\mathbf{g}_2$  as a first order multiple-variable Taylor series retaining only first-order terms, and recalling Eqs. A.1(f) and A.5, the following relation is obtained:

$$\begin{aligned}
\delta\mathbf{x}_{++} &= \mathbf{g}_2\{\mathbf{g}_1[\mathbf{x}(T_-), T_-]\} - \mathbf{g}[\mathbf{x}(T_-), T_-] + \\
&+ \left\{ \nabla\mathbf{g}_2^\top(\mathbf{x}, t) \Big|_{\mathbf{x}=\mathbf{g}_1[\mathbf{x}(T_-), T_-], t=T_-} \right\}^\top \mathbf{S}_1\delta\mathbf{x}_- + \\
&\left( \left\{ \nabla\mathbf{g}_2^\top(\mathbf{x}, t) \Big|_{\mathbf{x}=\mathbf{g}_1[\mathbf{x}(T_-), T_-], t=T_-} \right\}^\top \mathbf{A}\mathbf{g}_1[\mathbf{x}(T_-), T_-] \right. \\
&\left. - \mathbf{A}\mathbf{g}[\mathbf{x}(T_-), T_-] + \frac{\partial\mathbf{g}_2(\mathbf{x}, t) \Big|_{\mathbf{x}=\mathbf{g}_1[\mathbf{x}(T_-), T_-], t=T_-}}{\partial t} \right) \delta\bar{t}
\end{aligned} \tag{A.8}$$

where  $\delta\bar{t}$  is obtained as a function of  $\delta\mathbf{x}_-$  by use of the jump conditions, as follows. The jump conditions for the periodic and perturbed solution as related to the second impact are given by:

$$\begin{aligned}
h_2[\mathbf{x}(T_+), T_+] &= 0 \\
h_2[\bar{\mathbf{x}}(\hat{T}_-), \hat{T}_-] &= 0
\end{aligned} \tag{A.9}$$

Substituting Eqs. A.7(a), A.7(b), A.1(f) and A.5 into Eq. A.9(b), performing a first-order Taylor series expansion, and employing Eq. A.9(a), one obtains an equation relating  $\delta\bar{t}$  and  $\delta\mathbf{x}_-$ , which reads:

$$\delta\bar{t} = \frac{\{\nabla^\top h_2[\mathbf{x}(T_-), T_-]\}\mathbf{S}_1\delta\mathbf{x}_-}{\{\nabla^\top h_2[\mathbf{x}(T_-), T_-]\}\mathbf{A}\mathbf{g}_1[\mathbf{x}(T_-), T_-] + \frac{\partial h_2[\mathbf{x}(T_-), T_-]}{\partial t}} \tag{A.10}$$

Substituting Eq. A.10 into Eq. A.8, one obtains the following relations:

$$\delta\mathbf{x}_{++} = \mathbf{g}_2\{\mathbf{g}_1[\mathbf{x}(T_-), T_-]\} - \mathbf{g}[\mathbf{x}(T_-), T_-] + \mathbf{S}_2\mathbf{S}_1\delta\mathbf{x}_- \tag{A.11}$$

$$\mathbf{S}_2 \triangleq$$

$$\begin{aligned}
&\left\{ \nabla\mathbf{g}_2^\top(\mathbf{x}, t) \Big|_{\mathbf{x}=\mathbf{g}_1[\mathbf{x}(T_-), T_-], t=T_-} \right\}^\top + \left( \mathbf{A}\mathbf{g}[\mathbf{x}(T_-), T_-] \right. \\
&- \left. \left\{ \nabla\mathbf{g}_2^\top(\mathbf{x}, t) \Big|_{\mathbf{x}=\mathbf{g}_1[\mathbf{x}(T_-), T_-], t=T_-} \right\}^\top \mathbf{A}\mathbf{g}_1[\mathbf{x}(T_-), T_-] \right. \\
&\quad \left. - \frac{\partial\mathbf{g}_2(\mathbf{x}, t) \Big|_{\mathbf{x}=\mathbf{g}_1[\mathbf{x}(T_-), T_-], t=T_-}}{\partial t} \right) \times \\
&\quad \frac{\nabla^\top h_2[\mathbf{x}(T_-), T_-]}{\{\nabla^\top h_2[\mathbf{x}(T_-), T_-]\}\mathbf{A}\mathbf{g}_1[\mathbf{x}(T_-), T_-] + \frac{\partial h_2[\mathbf{x}(T_-), T_-]}{\partial t}}
\end{aligned} \tag{A.12}$$

The crux of the present derivation is embodied in Eq. A.11. The linear stability analysis performed here assumes a small perturbation in the solution prior to impact, and linear stability can only correspond to the perturbation staying small after the sequence of impacts has occurred. Consequently, a necessary condition for both the possibility of linear stability and the self-consistency of the linear stability analysis as a procedure is that the first two terms in the right-hand side of Eq. A.11 cancel out (formally they can result in an infinitesimal quantity, yet they contain no parameter taken to the limit zero in the context of the linear stability analysis and thus can only result in a finite value that thus has to be an exact zero), namely:

$$\mathbf{g}_2\{\mathbf{g}_1[\mathbf{x}(T_-), T_-]\} = \mathbf{g}[\mathbf{x}(T_-), T_-] \tag{A.13}$$

This consistency requirement can be termed 'impact-integrability', since it implies that a series of consecutive impacts produces the same result as a single synchronous impact. The collision of two bodies is always impact-integrable. However in the case of a simultaneous many-body impact, integrability may hold only given some restriction on the problem parameters, such that slight asynchronicity may not produce a finite change in the outcome. This intuitive observation is represented by formal linear stability analysis as shown above.

After revealed in essence for the two-impacts case, the requirement can be straight-forwardly generalized to  $n$  consecutive impacts, the induction

procedure appears trivial here. For a series of  $n$  impacts, the 'impact-integrability' requirement, or the necessary condition for stability would be:

$$\mathbf{g}_n[\dots(\mathbf{g}_2\{\mathbf{g}_1[\mathbf{x}(T_-), T_-]\} = \mathbf{g}[\mathbf{x}(T_-), T_-])] \quad (\text{A.14})$$

If indeed the system in question is impact-integrable, then it holds that by substituting Eq. A.13 into the first term in the parentheses in the expression for  $\mathbf{S}_2$  in Eq. A.12, it becomes apparent that the matrix  $\mathbf{S}_2$  is instantaneous and only depends on the value of  $\mathbf{x}$  *after* the first impact. Then it becomes clear that  $\mathbf{S}_2$  is a legitimate saltation matrix and one has:

$$\delta\mathbf{x}_{++} = \mathbf{S}\delta\mathbf{x}_-, \mathbf{S} = \mathbf{S}_2\mathbf{S}_1 \quad (\text{A.15})$$

for the two-impact case, and:

$$\delta\mathbf{x}_{+(n)} = \mathbf{S}\delta\mathbf{x}_-, \mathbf{S} = \mathbf{S}_n\mathbf{S}_{n-1}\dots\mathbf{S}_2\mathbf{S}_1 \quad (\text{A.16})$$

for the  $n$ -impacts case.

After establishing the impact-integrability requirement as the necessary condition for stability, it is left to note that in the setting assumed in section 2, there are only impacts between a mass and a wall, which is a two-body impact in essence, hence the aforementioned condition is satisfied automatically, and Eqs. A.12 and A.15 apply.

Also noteworthy is the following. The partial time derivatives of the jump conditions and the jump mappings appearing in Eqs. A.6 and A.12 can generally be non-vanishing, as, say, for the case of a periodically externally moved wall and a periodically externally controlled restitution coefficient (as in magnetorheological composites). Hence the corresponding terms (with the associated signs) may be of relevance. However, in the case considered in section 2, the walls are fixed and perfect restitution is assumed, for which the jump mapping is realized as a multiplication by a matrix. Consequently, Eqs. 13-15 are obtained.

## References

## References

- [1] S. Flach, D. Leykam, J. D. Bodyfelt, P. Matthies, A. S. Desyatnikov, Detangling flat band into fano lattices, EPL 105 (30001).
- [2] B. Luk'yanchuk, N. I. Zheludev, S. A. Maier, N. J. Halas, P. Nordlander, H. Giessen, C. T. Chong, The fano resonance in plasmonic nanostructures and metamaterials, Nature Materials 9 (2010) 707–715.
- [3] D. Leykam, S. Flach, O. Bahat-Treidel, A. S. Desyatnikov, Flat band states: Disorder and nonlinearity, Phys. Rev. B 88 (2013) 224203.
- [4] T. T. Heikkilä, N. B. Kopnin, G. E. Volovik, Flat bands in topological media, JETP Letters 94 (3) (2011) 233–239.
- [5] J. D. Bodyfelt, D. Leykam, C. Danieli, X. Yu, S. Flach, Flat bands under correlated perturbations, arXiv:1407.8345v2.
- [6] A. A. Ovchinnikov, Localized long-lived vibrational states in molecular crystals, Sov. Phys. JETP 30 (1) (1970) 147–50.
- [7] S. Flach, C. R. Willis, Discrete breathers: Advances in theory and applications, Phys. Rep. 295 (5) (1998) 181–264.
- [8] S. Flach, A. V. Gorbach, Discrete breathers: Advances in theory and applications, Phys. Rep. 467 (1) (2008) 1–116.
- [9] O. V. Gendelman, L. I. Manevitch, Discrete breathers in vibro-impact chains: Analytic solutions, Phys. Rev. E 78 (2) (2008) 026609.
- [10] O. V. Gendelman, Exact solutions for discrete breathers in a forced-damped chain, Phys. Rev. E 87 (6) (2013) 062911.
- [11] N. Perchikov, O. V. Gendelman, Dynamics and stability of a discrete breather in a harmonically excited chain with vibro-impact on-site potential, Physica D 292-293 (2015) 8–28.
- [12] P. Rosenau, J. M. Hyman, Compactons: Solitons with finite wavelength, Phys. Rev. Lett. 70 (38-39) (1992) 564.
- [13] Y. S. Kivshar, Compactons in discrete lattices, Nonlin. Coher. Struct. Phys. Biol. 329 (1994) 255–258.
- [14] O. M. Brown, Y. S. Kivshar, Nonlinear dynamics of the Frenkel-Kontorova model, Phys. Rep. 306 (1998) 1–108.
- [15] S. Dusuel, P. Michaux, M. Remoissenet, From kinks to compactonlike kinks, Phys. Rev. E 57 (2) (1998) 2320.
- [16] P. G. Kevrekidis, V. Konotop, A. Bishop, S. Takeno, Discrete Compactons: some exact results, J. Phys. A: Math. Gen. 35 (2002) L641–L652.
- [17] G. Gaeta, T. Gramchev, S. Walcher, Compact solitary waves in linearly elastic chains with non-smooth on-site potential, J. Phys. A: Math. Theor. 40 (2007) 4493–4509.
- [18] P. Rosenau, A. Zilburg, On a strictly compact discrete breather in a Klein-Gordon model, Phys. Lett. A 379 (43-44) (2015) 2811–2816.
- [19] J. D'Ambroise, M. Salerno, F. Abdullaev, P. G. Kevrekidis, Multidimensional discrete compactons in nonlinear Schrödinger lattices with strong nonlinearity management, arXiv (1508.03008).
- [20] M. Johansson, P. Jason, Breather mobility and the Peierls-Nabarro potential: Brief review and recent progress, Springer Series in Material Science 221 (Quodons in Mica) (2015) 147–178.
- [21] G. James, Periodic travelling waves and compactons in granular chains, J. Nonlin. Sci. 22 (5) (2012) 813–848.
- [22] P. Ndjoko, J.-M. Bilbault, S. Binczak, T. Kofané, Compact-envelope bright solitary wave in a DNA double strand, Phys. Rev. E 85 (0111916).
- [23] M. Johansson, U. Naether, R. A. Vicencio, Compactification tuning for nonlinear localized modes in sawtooth lattices, Phys. Rev. E 92 (2015) 032912.
- [24] Y. Zong, S. Xia, L. Tang, D. Song, Y. Hu, Y. Pei, J. Su, Y. Li, Z. Chen, Observation of localized flat-band states

- in kagome photonic lattices, *Optic Express* 24 (8) (2016) 8877–8885.
- [25] P. Müller, J. Richter, O. Derzhko, Hubbard models with nearly flat bands: Ground-state ferromagnetism driven by kinetic energy, *Physical Review B* 93 (2016) 144418.
  - [26] H. Ramezani, Flat band emerging from the exceptional point of a pt symmetric system, arXiv:1701.00291v2.
  - [27] L. Ge, Parity-time symmetry in a flat-band system, *Physical Review A* 92 (8) (2015) 0502103.
  - [28] A. Maimistov, On stability of flat band modes in a rhombic nonlinear optical waveguide array, arXiv:1607.07984v1.
  - [29] C. Poli, H. Schomerus, M. Bellec, U. Kuhl, F. Mortessagne, On stability of flat band modes in a rhombic nonlinear optical waveguide array, *2D Materials* 4 (2) (2017) 025008.
  - [30] M. Valiente, N. T. Zinner, Quantum collision theory in flat bands, *Journal of Physics B: Atomic, Molecular and Optical Physics* 50 (2017) 064004.
  - [31] C. Huang, F. Ye, X. Chen, Y. V. Kartashov, V. V. Konotop, L. Torner, Localization-delocalization wavepacket transition in pythagorean aperiodic potentials, *Scientific Reports* 6 (2016) 32546.
  - [32] S. Mukherjee, R. R. Thomson, Observation of robust flat-band localization in driven photonic rhombic lattices, arXiv:1703.07411v2.
  - [33] L. Morales-Inostroza, R. A. Vicencio, Simple method to construct flat-band lattices, *Physical Review A* 94 (2016) 043831.
  - [34] P. Jason, Theoretical studies of bose-hubbard and discrete nonlinear Schrödinger models - localization, vortices, and quantum-classical correspondence, Ph.D. thesis, Linköping University (2016).
  - [35] N. Perchikov, O. V. Gendelman, Nonlinear dynamics of hidden modes in a system with internal symmetry, *JSV* 377 (2016) 185–215.
  - [36] W. Maimaiti, A. Andreanov, H. C. Park, O. Gendelman, S. Flach, Compact localized states and flatband generators in one dimension, arXiv 1610 (2016) 02970.
  - [37] I. M. Merhasin, B. A. Malomed, Gap solitons in a model of a hollow optical fiber, *Opt. Lett.* 30 (2005) 1105–1107.
  - [38] M. di Bernardo, C. J. Budd, A. R. Champneys, P. Kowalczyk, *Piecewise-Smooth Dynamical Systems. Theory and Applications*, Springer, New-York, 2008.
  - [39] I. Grinberg, O. V. Gendelman, Localization in finite vibroimpact chains: Discrete breathers and multi-breathers, *Physical Review E* 94 (3) (2016) 032204.
  - [40] M. E. Hosea, L. F. Shampine, Analysis and implementation of tr-bdf2, *Applied Numerical Mathematics* 20 (1996) 21–37.
  - [41] O. V. Gendelman, T. Sapsis, Energy exchange and localization in essentially nonlinear oscillatory systems: canonical formalism, *Journal of Applied Mechanics* 84 (1) (2017) 011009.
  - [42] M. Abramowitz, I. Stegun, *Handbook of mathematical functions with formulas, graphs, and mathematical tables*, Dover Publications, 1964.